An automated approach to estimate carbon monoxide emissions from steel plants by utilizing TROPOMI satellite measurements

J.C.S. Anema

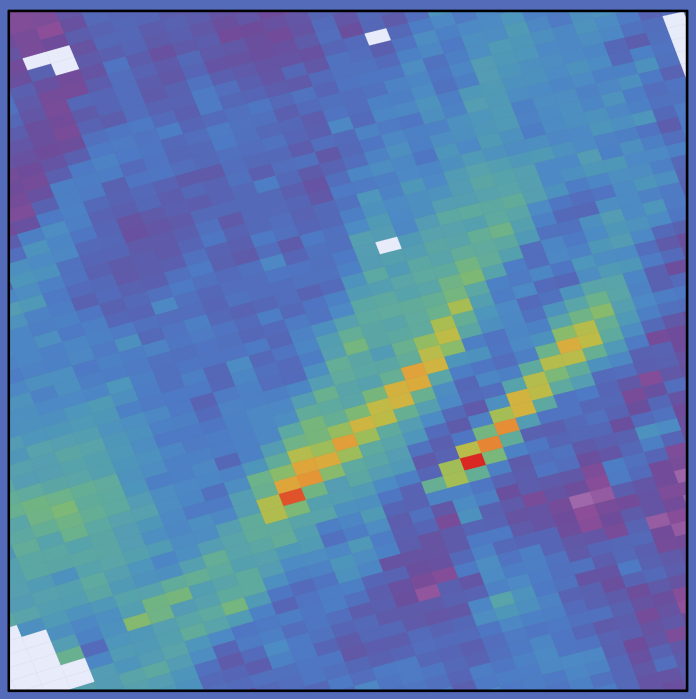

SRON
Netherlands Institute for Space Research

TU Delft

An automated approach to estimate carbon monoxide emissions from steel plants by utilizing TROPOMI satellite measurements

by

J.C.S. Anema

to obtain the degree of Master of Science
at the Delft University of Technology,
to be defended publicly on Wednesday February 3, 2021 at 09:00 AM.

Student number:	4276949	
Project duration:	December 1, 2020 – February 3, 2021	
Thesis committee:	Dr. S. Basu,	TU Delft CEG, chair & supervisor
	Dr. P. Veefkind,	TU Delft CEG
	Dr. D. Stam,	TU Delft AE
	Dr. T. Borsdorff	SRON, supervisor

An electronic version of this thesis is available at `http://repository.tudelft.nl/`.

Front page image: Visible plume structures from steel plant facilities (e.g. Ma'anshan and Benxi) located in the Liaoning Province, China, observed at 29-03-2020 by TROPOMI.

SRON Netherlands Institute for Space Research

TU Delft

Abstract

Since the 13th of October 2017, the Tropospheric Monitoring Instrument (TROPOMI) aboard ESA's Sentinel 5-Precursor (S5-P) satellite enables daily global measurements of carbon monoxide (CO) total column concentrations at an unprecedented spatial resolution of 7×5.6 km. TROPOMI has the ability to detect distinct pollution plumes, arising from point source emissions, from which emission rates can be derived. We investigate the potential of CO column concentrations observed by TROPOMI to estimate the CO emissions of point sources on an operational level. This study developed a Python framework that for pre-defined point sources automatically detects pollution plumes and from which it estimates CO emissions using a mass balance approach directly from single overpass CO observations. The algorithm is based on concepts from the computer vision to identify the plume and extract the plume center line while respecting the plume orientation. The emission rate is approximated from flux profiles through multiple plume cross-sections following the plume center line. The performance of the developed framework and its potential is demonstrated by the application on 132 identified steel plant facilities over a time period of more than 2.5 years. Currently the lack of accessible and quality-wise good data limits spatial or even temporal comparison of CO emissions from steel plants. Therefore the control and understanding of emission rates could greatly benefit from the proposed approach. In total we obtained 1,774 emission estimates for 97 facilities. Up to 119 measurements per facility are derived where for the majority of the facilities the average number of measurements is around 10. The obtained time series showed large variation in the distribution of measurements over time as well as the emission values itself. For a number of higher emission values, that exceeded up to 2 times the average emission, measured for e.g. the Bhilai Steel Plant, India, the outliers corresponded with interference of another source. Although individual plumes could be identified for two sources (~35 km apart) in the same Bhilai area, no non-merged plumes were detected for the Schwelgern and Huttenheim sites (~18 km apart) in Duisburg, Germany. Moreover, we tested the agreement of our measurements with recorded or stated events: i) The emission estimate from the afternoon of the 24th of May 2019, Bhilai site, confirmed the manufacturers statement that the operations had continued that day despite a reported fire in the morning. ii) Our results did not match the significant global drop noted in steel production during the first period of 2020 as a result of the pandemic. The scattered distribution of measurements and their emission values over time seem to limit the representation of a small time frame needed for such analysis. iii) We found a positive correlation with a Pearson Coefficient of 0.76 between the European Pollutant Release Transfer Register (E-PRTR) and our data. For all examined facilities our obtained emissions were greater than reported by the facilities to E-PRTR. This might indicate an underestimation of the data registered. This first evaluation emphasizes the potential of TROPOMI observations to improve our understanding of point source emissions and to compliment existing data such as the E-PRTR. However, to be able to interpret the data from TROPOMI indeed structurally and to develop a reliable validation method extensive data-analysis on plant and area-level is required, especially to be able to rule out interfering factors.

Preface

This master thesis is part of the Environmental Engineering MSc programme at the Faculty of Civil Engineering and Geosciences at the TU Delft. This thesis research was done in cooperation with the Earth Sciences department at SRON (Netherlands Institute for Space Research).

The launch of TROPOMI in 2017 sparked my specific interest in working with satellite data for the purpose of atmospheric monitoring. The possibilities and potential that arises from TROPOMI's daily global mapping for monitoring of several key atmospheric constituents inspired me to specialize into the field of remote sensing. Being able to work with this data and explore its potential for the use of air quality monitoring has been a wonderful and sometimes challenging experience.

First of all, I am thankful for the opportunity to work with the team at SRON. Specifically I would like to thank my supervisor Dr. Borsdorff for the great brainstorm sessions that we have had, his guidance and support during the entire thesis. I wish to thank Dr. Basu, my university supervisor, for all his patience and great advise along the way. I also would like to thank Dr. Goudar for his enthusiasm during our discussions and his advice on programming. Furthermore, I would like to thank the other SRON colleagues for their feedback on my work during the meetings.

Juliëtte Anema
February 2021

Contents

1. Introduction

Since the 13th of October 2017, TROPOMI (TROPOspheric Monitoring Instrument) contributes to space-born atmospheric measurements by enabling daily global observations at an unprecedented spatial resolution. TROPOMI is a multispectral grating spectrometer measuring the reflected solar radiance by the Earth surface and atmosphere from the ultraviolet (UV), visible (VIS) to the near-infrared (NIR) and shortwave infrared (SWIR) [Veefkind et al., 2012]. The instrument is the single pay-load of ESA's Sentinel-5 Precursor (S5-P) satellite dedicated to support policy-makers as part of Europe's Earth observation program Copernicus [Aschbacher and Milagro-Pérez, 2012]. Carbon monoxide (CO) is one of the main targets from TROPOMI and is retrieved from the shortwave infrared (SWIR) range (2.3μm) enabling sensitivity to boundary layer level [Landgraf et al., 2016]. TROPOMI provides daily global CO measurements with a spatial resolution of about, recently, 5.5×7 km^2 (across × along track) [Van Kempen et al., 2019]. In addition, the high signal to noise ratio allows the use of data from single overpasses for the detection of CO enhancements [Borsdorff et al., 2018]. The data quality of TROPOMI improves significantly on the SWIR measurements offered by predecessor SCIAMACHY (SCanning Imaging Absorption spectroMeter for Atmospheric CartograpHY) with a spatial resolution of 30×120 km and global coverage cycle of 3 days [Bovensmann et al., 1999].

Continuous frequent global measurements of carbon monoxide concentrations are of great importance to improve the understanding of tropospheric chemistry and for the purpose of air quality monitoring. Carbon monoxide (CO) is mainly released through incomplete combustion and concerns public health [Levy, 2015, Nigam et al., 2010, Raub et al., 2000] and in-directly radiative forcing by affecting the oxidation capacity of the atmosphere as a result of reacting with dominant sink [Holloway et al., 2000] hydroxyl radical (OH) [Khalil and Rasmussen, 1984, Wofsy et al., 1972]. Monitoring of CO provides valuable information regarding pollution trajectories of CO emitted sources due to the relatively long preservation of the trace gas, ~1-3 months, and low background concentration [De Laat et al., 2001, Holloway et al., 2000, Shindell et al., 2006].

From the first CO space-born measurements in 1989 by MAPS [Connors et al., 1999], satellite observations accelerated the understanding of spatial and temporal trends in CO concentrations (e.g. seasonal biomass burning) [Mallik and Lal, 2014, Spichtinger et al., 2004, Yadav et al., 2017]. TROPOMI facilitates the detection of small scale emissions, e.g. cities [Borsdorff et al., 2018, 2019], roads [Borsdorff et al., 2019], industries [Reuter et al., 2019] and fires [van der Velde et al., 2020] and therefore enables new opportunities for air pollution monitoring. Atmospheric satellite measurements provide the integrated concentration over a vertical column. The interpretation of plumes and the assigning to the specific source is a critical step to estimate emissions with the help of satellite observations [Varon et al., 2018]. Recent studies [Kuhlmann et al., 2019, Lorente et al., 2019] demonstrated the possibilities of the use of inversion techniques to obtain emission estimates using satellite measurements.

The amount of incoming data together with the large number of detectable sources make visual inspection to distinguish plumes limit operational applicability as a result of its computational expense [Kumar et al., 2020, Thompson et al., 2017]. An automatic approach will be necessary to reach the full potential of the data and contribute to mapping of CO emissions.

Steel plants are a primary example of anthropogenic point sources detectable by TROPOMI [Reuter et al., 2019, Schneising et al., 2019] which could benefit from an automatic operational system that estimates carbon monoxide emissions. Accessible high quality data is sparse and the inconsistency of applied measurements or estimation techniques limits the incomparability of CO emissions among steel facilities or even over time [Dios et al., 2013, Mennen et al., 2008, Pulles, 2008]. The European Union regulates emissions by setting integral permits based on Best Available Techniques (BAT) as key protocol of the Integrated Pollution Prevention and Control (IPPC) guidelines set by the United Nations Framework Convention on Climate Change

(UNFCCC). Even though the BAT is implemented widely [Mennen et al., 2008, Shatokha et al., 2020], the emission efficiency of plants worldwide deviates strongly with the difference in recycling of CO-rich gasses as one of the causes [Streets et al., 2006, Wang et al., 2016].

This study aims to contribute to the development of operational emission estimation systems by the development of a framework that automatically identifies pollution plumes and interprets the emission rate using the plume enhancement from single overpass TROPOMI CO data. We will focus specifically on the monitoring and analysis of CO emissions from worldwide steel plants. To our knowledge, this is the first study to map CO emissions from a large number of globally distributed steel plants directly interpreted from space-born CO data using an automatic detection system. This work consists of two main steps: (1) the development of a robust framework that enables carbon monoxide emission estimates over time from a pre-defined point source and (2) the analyses of the potential of such framework to improve the understanding of CO emissions from steel plants worldwide. We propose a new plume detection method utilizing computer vision concepts that particularly targets at the segmentation of small individual plumes as opposed to statistical approaches used by previous studies [Kuhlmann et al., 2019, 2020, Varon et al., 2018]. The emission estimation is computed through the mass-balance approach, which integrates the CO mass flux over plume transects perpendicular to the flow [Krings et al., 2013, Lavoie et al., 2015, Reuter et al., 2019]. The framework is applied on a large number of steel plants and processed for over 2.5 years, between mid-November 2017 and mid-August 2020, of total CO column concentrations observed by TROPOMI. The analysis of the potential of the new obtained data will mainly focus on the ability to compare emissions, detect changes over time and the agreement with known events or emission records for validation purposes.

An overview of the field concerning emission estimations from satellite observation is provided in chapter 2. The used data sets and methods, including the developed framework, are covered, respectively, in chapters 3 and 4. The results covering the performance of the framework as well as the analysis are presented in chapter 5, whereafter the discussion and conclusion are covered in chapter 6.

2. Literature

Consistent and solid measurements of trace gas emissions into the atmosphere are necessary to efficiently manage and utilize policies and protocols aiming at reducing anthropogenic emissions to act on the recent concerns regarding global warming and air pollution [Janssens-Maenhout et al., 2020, Mennen et al., 2008, World Health Organization, 2016]. Over the last decade, the use of satellite observations emerged into a promising approach to compliment conventional bottom-up emissions [Kourtidis et al., 2018, Streets et al., 2013]. Space-borne measurements of the atmospheric composition rose as an important resource that could improve emission quantification of multiple trace gases [Streets et al., 2013]. The strength of satellite observations lies in the providing of continuous global measurements. Frequent global measurements allow capturing of rapidly changing emission patterns due to e.g. fast growing economies [Kourtidis et al., 2018], application of emission reducing techniques [Li et al., 2010], occurring of a crisis [Krotkov et al., 2016, Liu et al., 2020] or sudden events such as volcanic eruptions [Ge et al., 2016] and gas leakages [Pandey et al., 2019]. With the revolutionary development of high resolution measurements in combination with high signal to noise ratio from instruments such as TROPOMI, single overpasses can reveal plume structures without the need for temporal averaging [Beirle et al., 2019, Broquet et al., 2018, Kuhlmann et al., 2020], as presented in figure 2.1.

Satellite based atmospheric measurements cover the trace gas concentration over a vertical column of air. In order to verify the use of the columnar concentrations for emission quantification, transport mechanisms and chemical activity should not greatly affect the concentration in the plume [Streets et al., 2013]. Inversion techniques are used to convert the observed vertical integrated concentrations to emission rates through simulations and assumptions of the transport that distributed the incoming flow. The approaches could be distinguished into the application of transport simulation models and techniques solely based on the observed enhancement. The latter, are especially appropriate and used for the interpretation of distinct plumes such as the steel plant plumes presented in figure 2.2. The unknown wind field is a common factor of uncertainty [Varon et al., 2018].

Inverse modeling is a commonly used method where atmospheric observations are combined with Chemical Transport Models (CMTs) to quantify emissions to the atmosphere. In the case of a long lifetime compared to the transportation, e.g. CO in sub-city scale [Borsdorff et al., 2020, Dekker et al., 2017], chemical degradation is often assumed negligible and only the transportation processes are taken into account. The models simulate the affect of atmospheric processes on the emitted gas, whereas the observation data is used to adjust the priori input set as emission rate. Brunner et al. [2019] studied the sensitivity of inversion modeling to the vertical allocation of CO_2 emissions. According to Brunner et al., the placement of the source should be represented in all three-dimensions and an incorrect assumption of surface emission could lead to uncertainties in the modeled concentration. Emissions from most point sources are emitted from stacks The effective emission height depends on the stack height of point sources as well as the rise of the plume after its release into ambient air. The ability to rise depends on the thermal buoyancy as well as the supplied vertical moment [Seinfeld and Pandis, 2016]. The importance of source properties for atmospheric dispersion modeling was also indicated by other studies, e.g. Pregger and Friedrich [2009] and Matthias et al. [2018]. Furthermore, Borsdorff et al. [2019] mentioned the difficulty of the application of the WRF model on small sub-city scales.

Besides the application of complex or simplified inversion models, the flow rate can be estimated directly from the satellite observations by methods such as the mass balance approach. Following the approach, the emission rate must equal the mass discharged through the cross-sectional area per unit of time under the

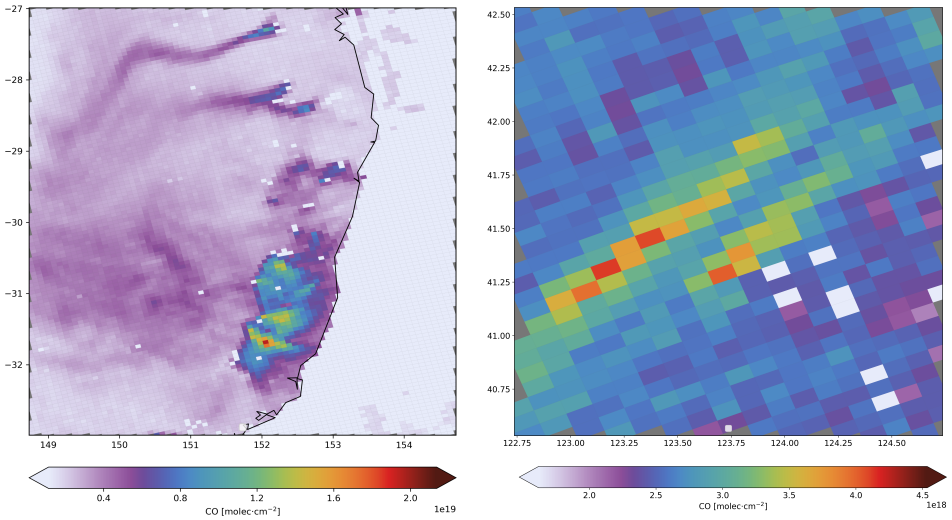

Figure 2.1: Plume structures visible in TROPOMI CO data, originated from (left) wild fires in Australia at 18-11-2020 and (right) steel plant facilities located in Benxi (China) at 02-06-2018.

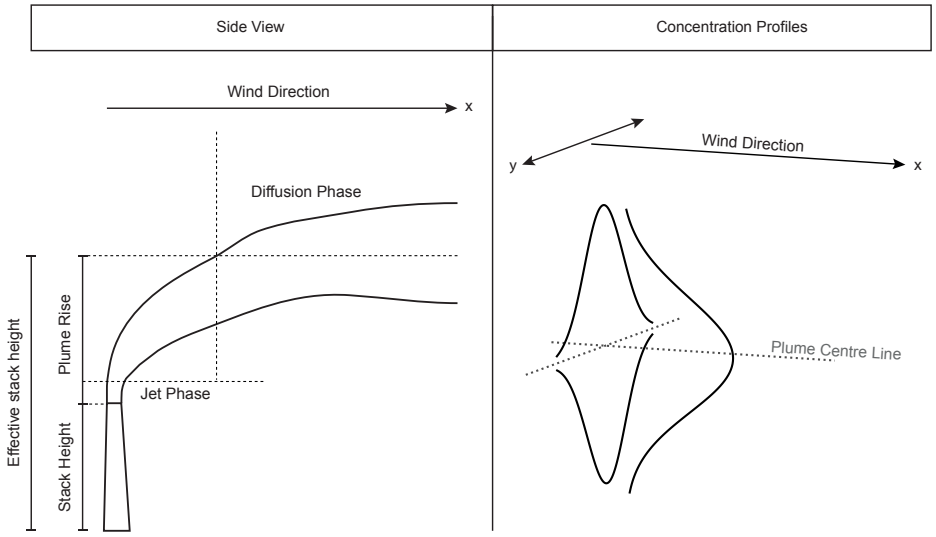

Figure 2.2: Representation of plume dynamics. The left image illustrates the rise of the plume after the injection in the atmosphere from the stack. After the final plume rise the plume follows the wind direction. The right images illustrates the concentration profile of the cross-sections of a plume.

assumption of a steady-state condition [Gordon et al., 2015, Kuhlmann et al., 2020, Reuter et al., 2019]. In the literature the mass balance is frequently applied, both on in situ (e.g [Cambaliza et al., 2015, 2014, Trainer et al., 1995, White et al., 1976]) and remote sensing (e.g. [Krings et al., 2013, Reuter et al., 2019]) observations, for emission estimations from cities [Kuhlmann et al., 2020] as well as from single point sources [Lavoie et al., 2015]. The application of the approach on space-borne observation benefits from the capturing of the total plume concentration in the columnar measurements [Varon et al., 2018]. An estimated wind speed is used to describe the advection.

However, the unknown wind speed remains a large uncertainty factor. The parameterization of the wind speed as the plume driving force (advection) neglects the diffusion by turbulent eddies. Therefore interpretation of the emission rate by the mass balance approach is only appropriate for advection-dominated plumes under steady-state condition According to Reuter et al. [2019], discrepancy between the true and interpreted source rate could arise from variation in the wind speed and direction from the time of emission until the plume observation. The method should not be applied on low wind conditions, smaller than 2 m/s according to literature (e.g. Denmead et al. [1998], Sharan et al. [1996], Varon et al. [2018]), due to high variability and possible occurrence of vertical plumes. In addition, the influence of chemical reactions on the balance should be taken in to account for chemical active trace gases such as NO_2 [Reuter et al., 2019].

To locate the plume and its path, Varon et al. [2018] and Kuhlmann et al. [2020] detected the enhanced pixels, identifying as plume, using statistical tests.

3. Description of Data Processing

3.1. CO Column Concentrations observed by TROPOMI

This study uses the TROPOMI Level-2 CO product from November 2017 to mid August 2020. The vertical integrated CO density from TROPOMI is inferred from solar backscatter measurements in the Shortwave Infrared (SWIR) spectral range at 2.3 μm [Landgraf et al., 2016].

TROPOMI is a nadir viewing push broom image spectrometer with a swath (across-track) covering 2600 km and a two-dimensional detector plane. The instrument slit is imaged on the two-dimensional detector and sampled in spectral and spatial dimension [Veefkind et al., 2012]. The ground view of the SWIR spectrometer covers 3.4×7 km^2 respectively in flight and across flight direction [Landgraf et al., 2016]. Temporal integration over 1 s in the flight direction results in ground pixel sampling of ~7×7 km^2 [Landgraf et al., 2016]. From the 6th of August 2019, the ground pixel resolution is improved to 5.5×7 km^2 due to a decreased readout time of the detectors [Borsdorff et al., 2020]. Figure 3.1 provides an overview of the principle.

Finally, the Shortwave Carbon Monoxide Retrieval (SICOR) [Landgraf et al., 2018, 2016, Vidot et al., 2012] algorithm is deployed to infer the total columns from the 2324-2338 nm window (covering absorption band of CO). From this spectral range, the interference of atmospheric scattering is limited under clear-sky conditions enabling sensitivity to the boundary level [Landgraf et al., 2016]. Prior to the retrieval of the CO total column, observations that are strongly contaminated by optically thick clouds or that have a too low solar radiance signal are rejected [Landgraf et al., 2018]. Large inland waters or oceans may not scatter enough light necessary for the retrieval under clear sky conditions.

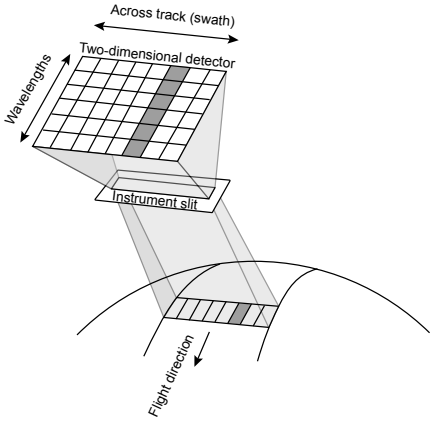

Figure 3.1: The two-dimensional detector and instrument split with respect to the ground pixels. Image altered from [Veefkind et al., 2012] and [Landgraf et al., 2016].

From the nominal operation phase (E2) [Van Kempen et al., 2019], since 1 May 2018, the processing of the TROPOMI L2 data is operational and comprises 14 orbits per day with a repeat cycle of 16 days. The original data product is structured per satellite orbit or per granule (section of an orbit) and stored in NetCDF4 files. We restructured the data in equal blocks distributed over space (using cylindrical equal-area projection) and time to allow rapid extraction of data covering the geographical area of interest. Figure 3.2 illustrates the data

structured per orbit and as proposed by this study. We only selected sub-data (e.g. CO total column concentrations, geolocation information of ground pixels, time) necessary for processing for storage in the DDS. The selected data was limited to observations over clear-sky or mid-level cloud (<5,000 m) conditions and with a Solar Zenith Angle (SZA) smaller than 80°. The strong influence on the light path due to interference of clouds or under low sun conditions (SZA<80°) (longer light path) could result in higher errors in the data. Clear sky and mid-level cloud scenario's are indicated by the aerosol optical depth (τ_{aer}) and cloud layer height (z_{cloud}) as shown in equation 3.1 [Landgraf et al., 2019]. Furthermore, the most westward pixels were masked due to unresolved calibration issues [Landgraf et al., 2019]. The columnar CO data obtained from the TROPOMI L2 product consisted of stripes occurring in the flight direction. These stripe patterns are deemed erroneous (<5%) [Borsdorff et al., 2018, Landgraf et al., 2019]. It was noted that the false elongated pattern of the stripes could hamper the plume detection, therefore we corrected for the stripes by applying a median filter as suggested by Landgraf et al. [2019].

$$\begin{aligned} &\text{Clear Sky} && \tau_{aer} < 0.5 \;\&\; z_{cloud} < 500\text{m} \\ &\text{Mid-level} && \tau_{aer} \geq 0.5 \;\&\; z_{cloud} < 5,000\text{m} \end{aligned} \tag{3.1}$$

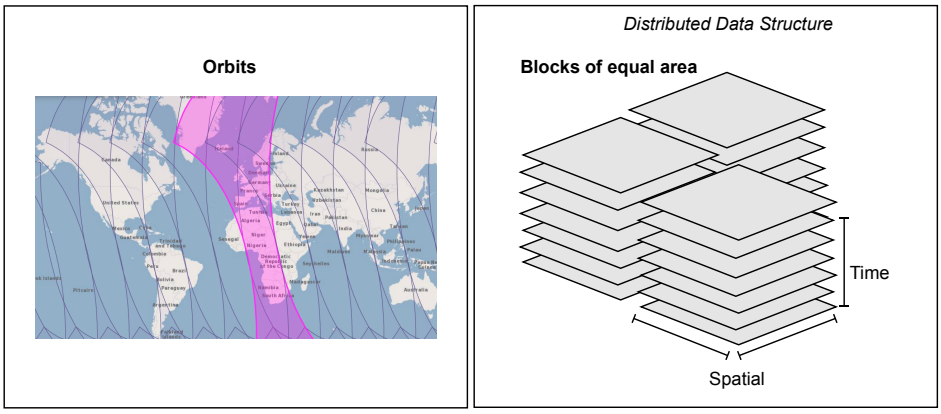

Figure 3.2: Representation of the data stored per orbit (TROPOMI L2 files) and structured in blocks distributed equally over space and time as done in this study. The left image was extracted from `https://s5phub.copernicus.eu/`

3.2. Detection of Steel Plant Facilities

A list of steel plants and their specific coordinates to use as case studies and input was obtained through several searching techniques. First of all, we searched for steel work locations using information provided on larger steel manufacturers websites (e.g. ArcelorMittal, Steel Authority of India Ltd. (SAIL) and Nippon Steel Corporation) and international emission inventories (e.g. National Emissions Inventory (NEI) and European Pollutant Release Transfer Register (E-PRTR)). Not all countries register emissions or indicate the emissions per individual facility in inventories (or in accessible inventories). The detection of plumes using the obtained algorithm was found to be limited and difficult for steel plants with a noted annual CO emission below ~30,000 tonnes. Therefore, steel plants with accessible annual CO emission and emissions above the threshold of 30,000 tonnes were listed. Notice that the activity of steel plants could change over time and therefore could deviate from what is stated in the inventories when the data corresponds to a previous year. Both approaches were limited and time consuming as a result of language-barriers and lack of information. Therefore, we detected most steel plant locations visually using the VIIRS I Band 375 m Active Fire Product (VNP14IMG) [Schroeder and Giglio, 2018] from the Fire Information for Resource Management System (FIRMS). Thermal anomaly products, e.g. VNP14IMG, reveal prominent heat sources such as combustion activities at steel works [Liu et al., 2018, Ma et al., 2018, Zhou et al., 2018]. The product from VIIRS / Suomi NPP (Suomi National Polar-orbiting Partnership) was used, rather than VIIRS / NOAA-20, because of the benefit of flying in close formation of S5-P with S-NPP [Veefkind et al., 2012]. To optimize the visual inspection of steel work locations the VNP14IMG data with a temporal coverage of several weeks, preferably outside the fire seasons, has been viewed on a background of World Imagery [ESRI et al., 2018] as illustrated in figure 3.4.

The obtained locations were verified as steel plants by using recent Google Earth images (figure 3.5).

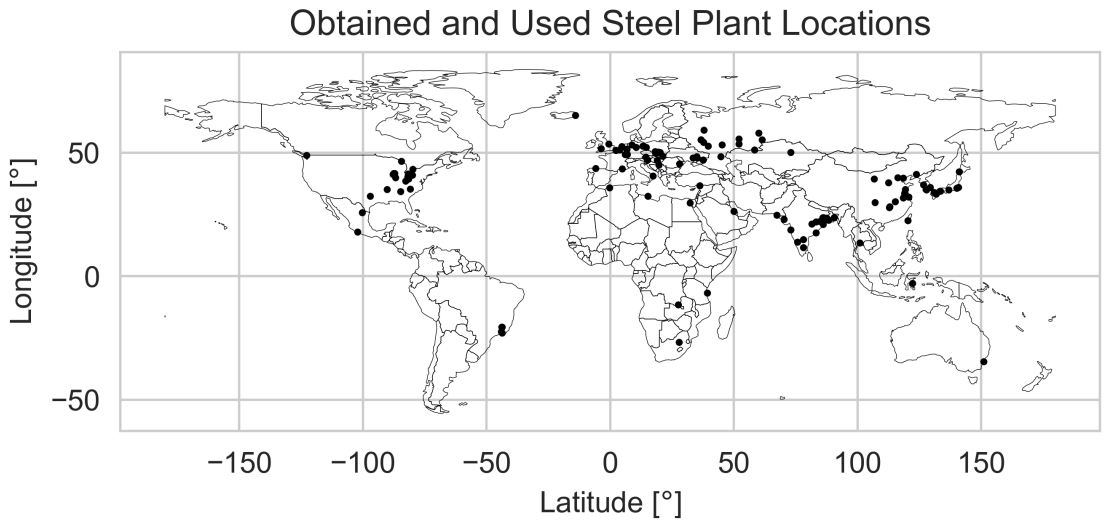

Figure 3.3: Locations of the 132 steel plants listed and analyzed by this study.

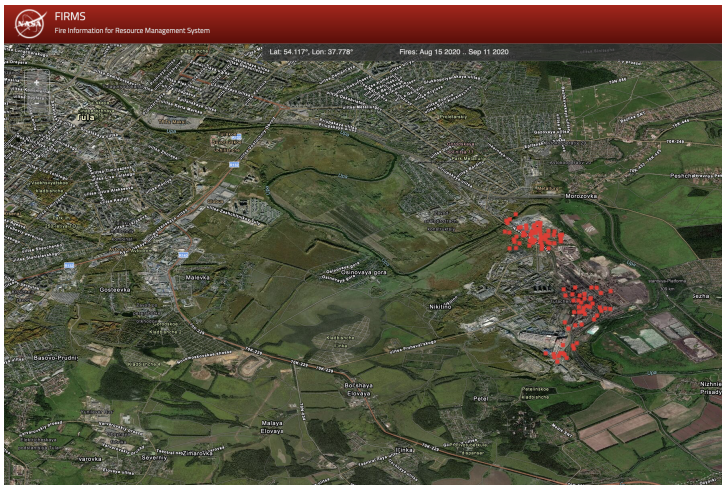

Figure 3.4: Visual detection of steel plants with help of VNP14IMG data plotted on World Imagery map from FIRMS (`https://firms.modaps.eosdis.nasa.gov/map/`). Example shows steel plant located in Tula, Russia (54.16°, 37.73°) with VNP14IMG data covering from 15-08-2020 until 11-09-2020.

The identification of plume structures over time relies on the occurrence depending on meteorological conditions as well as the operational cycle of the specific source. In order for TROPOMI to capture the plume information the occurrence of the plume should align with the time of overpassing. Furthermore, the enhancement of the plume among the background needs to be in the range of the precision of the instrument. This study did not focus on the detection limits. To obtain the number of overpasses (from November 2017 - Mid August 2020) for each location, all lit sides of orbits overpassing the 1°×1° area around the source point were counted. Figure 3.6 shows the number of overpasses over each steel plant and the percentages of the overpasses suitable for the detection. The suitability of an overpass for plume detection depends on the number of masked pixels (due to cloud contamination or clear conditions over sea) and the ground pixel sizes (maximum 15 km in swath direction). A minimum of 16 pixels covering the 1°×1° area is required to run the algorithm. Notice that the threshold of 16 pixels is not necessarily the amount of pixels from which plumes can be detected from the area. From figure 3.6, the gradual increase in number of overpasses toward the higher latitudes (N and S) is apparent. Whereas, the percentages of accepted overpasses were more spatially scattered. The facility located in Fjarðabyggð(Iceland), a region known for the high annual cloud cover

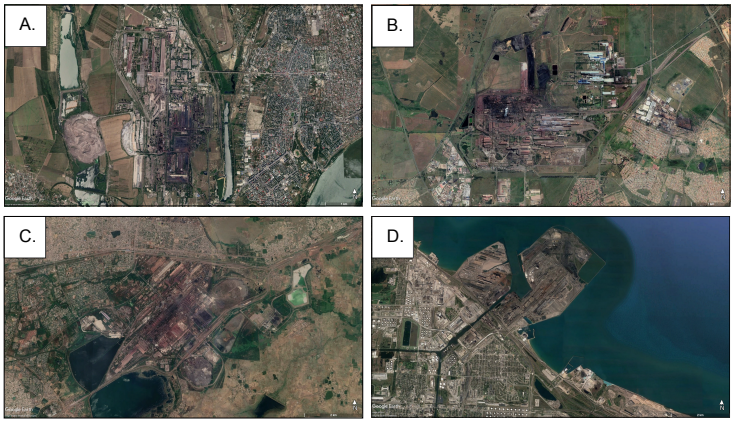

Figure 3.5: Google Earth imagery was used to validate the obtained locations of steel plants. A)Galaţi steel works, Romania (45.42°, 27.98°), B) Vanderbijlpark steel works, South-Africa (-26.66°, 27.82°), C) Bhilai steel plant, India (21.19°, 81.39°) and D) Indiana Harbor steel facility (East Chicago), USA (41.67°, -87.45°)

fraction, counted the highest number of overpasses (3602) and at the same the lowest rate (~0.50%) of cases suitable for the detection algorithm.

To obtain more understanding regarding the CO emitted by steel processes, we contacted steel facilities of Arcelor Mittal and thyssenkrupp respectively located in Gent (Belgium) and Duisburg (Germany). Furthermore, information about the production processes facilitated at each steel plant and the annual production of crude steel were mainly found from annual reports published by steel manufactures. Notice that the amount of easy accessible information regarding the facilities deviated strongly per manufacturer and country.

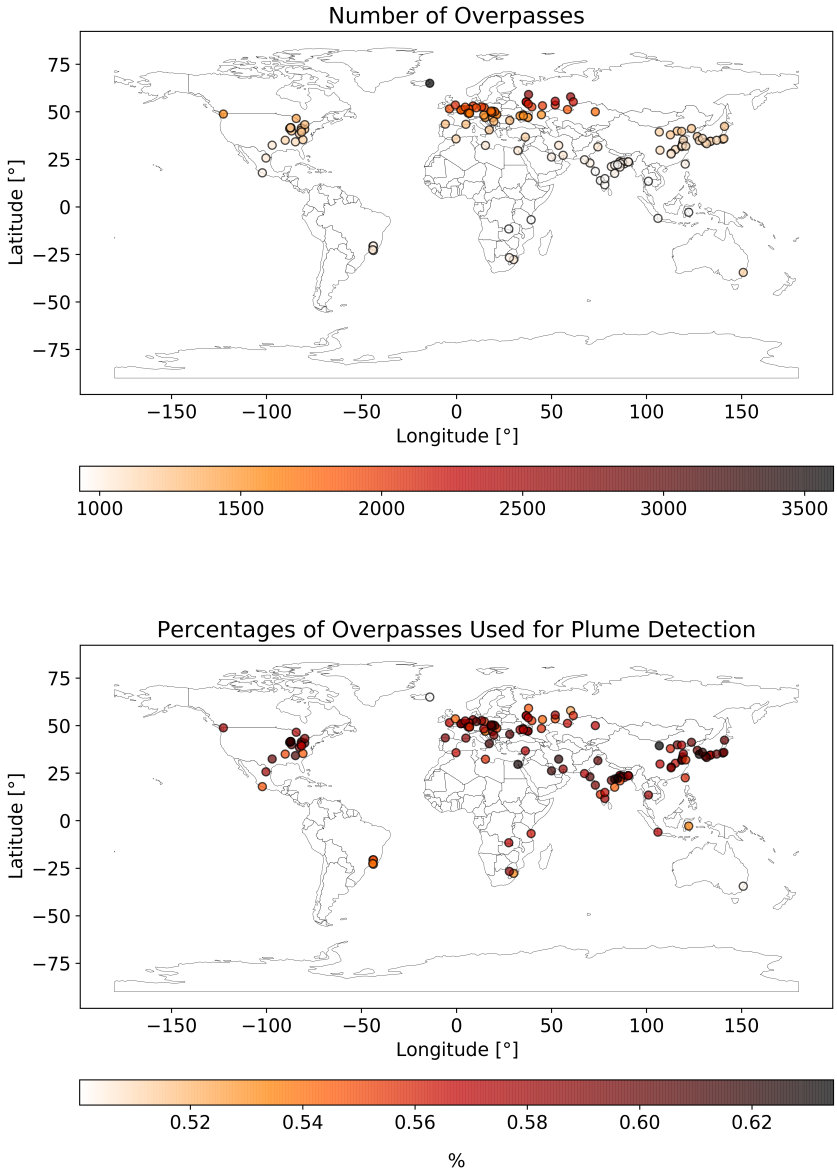

Figure 3.6: Number of overpasses, under day conditions, over each steel plant area and the percentage of those overpasses that met the criteria, maximum ground pixel width (across track) of 15 km and minimum of 16 non-masked pixels, for the applicability of the framework. The steel plant area is defined as 1°×1° around the steel plant. Data from November 2017 - Mid August 2020 is covered.

3.3. ERA5 Wind Fields

ERA5 [C3S, 2017] contains global reanalysis data covering 4D atmospheric data produced through data assimilation by the European Centre for Medium-Range Weather Forecasts (ECMWF) [ECMWF, 2020]. In this study the hourly single level, 10 and 100 meter, wind component data at the high resolution of 0.25°×0.25° (~27.75×27.75 km) will be used.

3.4. Pollutant Release and Transfer Register (PRTR)

This study makes use of the European Pollutant Release and Transfer Register (E-PRTR) for validation purposes. The European Commission implements the Pollutant Release and Transfer Register (PRTR) protocol through the E-PRTR. The register contains reported data pollution by over 30,000 industrial facilities from the 27 European Union Member States as well as the UK, Iceland, Liechtenstein, Norway, Serbia and Switzerland and is accessed through `https://prtr.eea.europa.eu/`. The latest E-PRTR data refers to the year 2017.

It should be noted that the emissions could have changed over time since the last reporting. The E-PRTR only provides information regarding the annual emissions of the point sources and the dominant activity. Information regarding the amount of production, specific facilities or site location is not given.

The United Nations Economic Commission for Europe (UNECE) Pollutant Release and Transfer Register (PRTR) protocol to the Aarhus convention facilitates public access to the release and transfer of 86 substances from 64 activities [United Nations, 2007]. The protocol was adopted in Kiev on 21 May 2003 and signed by 36 countries and the European Community. It is designed as an open global protocol. All members are required to collect reported data from facilities in national registers and to establish public access to the annual emissions per substance, activity and facility [European Commission, 2006, United Nations, 2007].

The PRTR supports insight into emissions from the participating countries [Kolominskas and Sullivan, 2004, Tang and Mudd, 2014]. However, the PRTR data is policy oriented and could diverge from national inventories and the true scientific emission rates [Pulles, 2008]. The quality is difficult to asses due to varying reporting methods and assumptions per facility and over time [Dios et al., 2013, Saarinen, 2003]. Therefore, limitations arise from the quality and the incomparability of emissions among facilities or over time [Dios et al., 2013, Mennen et al., 2008, Pulles, 2008]. Despite the unknown scientific quality of the data, the PRTR are the only more or less complete free available data sets [Pulles, 2008].

4. Methods

This study developed a framework that automatically detects and thereafter estimates the emission from point sources directly from satellite observations. The emission estimation makes use of the mass balance approach. The framework is designed and tested on numerous case studies covering plumes from steel plants facilities around the world using TROPOMI L2 CO data. The framework makes use of several fixated thresholds with values empirically found. Figure 4.1 illustrates the steps taken in the framework. Where the white and grey blocks, respectively, refer to the input data and individual algorithms. The framework is written in python and designed to rapidly detect plumes from a pre-defined point source over each overpass. To allow rapid processing, the L2 CO data (originally stored per orbit) is restructured in the form of data blocks distributed over space and time.

The framework returns the CO source rates of a specific point source over time. The first step covers the detection and segmentation of the plume area from a 1×1 ° area around the source location (subsection 4.1). Whereafter, the center line of the plume area is extracted (subsection 4.2). The center line is used to find the plume transects perpendicular to the plume direction. The methods applied for the segmentation and center line extraction are commonly used for blob detection purposes, such as the detection of retinal vessels [Bankhead et al., 2012, Kumar et al., 2016], pathology detection [Kong et al., 2013] and land-water boundary detection [González-Jorge et al., 2018]. The identification of plumes as a coherent group of pixels significantly enhanced among the background enable the use of blob detection. Once the center line is found, multiple transect perpendicular to the line are obtained. Using, on quality selected, transects, the source rate is estimated by the mass balance approach using ERA-5 re-analysis 100 m wind data (section 4.3). Once the emissions over time are estimated, the plume enhancement will be tested among the general background variation and post-processing will be done to eliminate falsely or poor quality detected cases (section 4.4). The discarding of cases/measurements takes place during the iteration process over all orbits and after the processing. Although, the testing of the plume enhancement is seen as last part of the detection algorithm rather than a post-processing step, the criteria was tested after the running for all orbits since the location specific threshold is estimated from the time series.

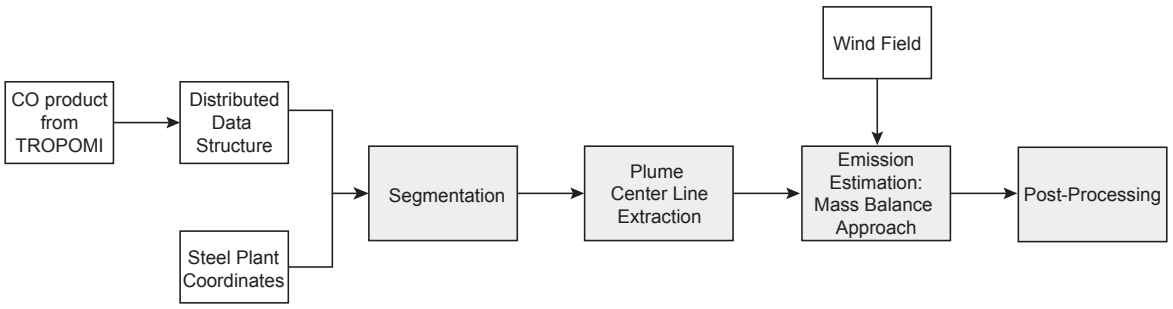

Figure 4.1: Overview of the obtained automatic detection and emission estimation algorithm. Level 2 CO data from TROPOMI is structured to allow rapid reading and together with steel plant coordinates used as input. ERA-5 reanalysis wind data is used as input for the emission estimation.

4.1. Plume Detection Algorithm

Key to the developed framework is the plume detection algorithm. The algorithm consists of three main steps (as shown in figure 4.2) and combines the application of image processing techniques and a statistical test. Prior to the actual detection, the CO total column concentrations and data covering the geolocation of the pixels are read from the data structure (discussed in 3.1). The data is transformed to a 2D matrix, with the position of the pixels representing the order of recorded ground pixels over the orbit. The rows and columns represent the swath (across track), consisting of 215 pixels [KNMI, 2019], and the covered orbit (see figure 3.1). A selected area of 1×1° with the source point as its center is used. The small area limits the capturing of adjacent sources and spatial patterns. Furthermore, the variation of ground pixel sizes in the swath will be minimal. Figure 4.3 presents a selected area of 1×1° (~111×111 km) around a source point of interest transformed to a 2D matrix.

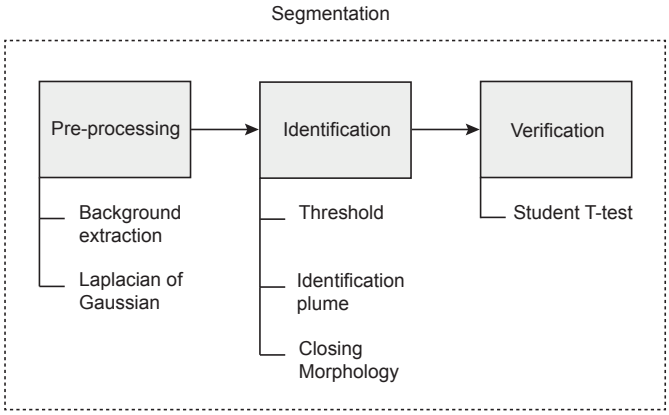

Figure 4.2: Overview of the processes used for segmentation of the image into surrounding and plume pixels linked to a specific source point.

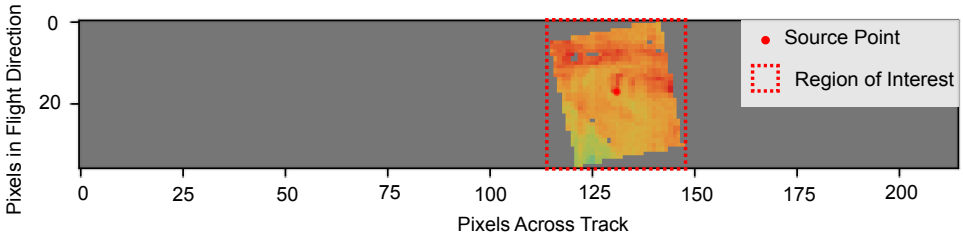

Figure 4.3: Extracted area of 1×1° around the source point represented as a 2D matrix respecting the order of recorded ground pixels. The x-axis refers to the number of pixels across the track with a total of 215 pixels covering the entire swath. The y-axis refers to the pixels in the flight direction. The red dashed square represents the area that will be cropped to limit the matrix to the region of interest.

The algorithm for the plume detection, or segmentation, starts with the pre-processing step. In this step the contrast between plumes and the background is intensified to ease thresholding. Figure 4.4 presents the steps taken. First of all, the local enhanced areas are eliminated by subtracting an estimated background from the image. The background is approximated by the application of a median filter. The mean filter replaces each pixel value by the median of the pixels values captured by the sliding window, such that:

$$I'(x,y) = \text{median}(\{I(x+i, y+j) | (i,j) \in W\}) \tag{4.1}$$

where I and I' represent the original and filtered image, (x,y) are the indices of a specific pixel and (x+i,y+j) are the indices of the neighboring pixels captured by window W. If the window size exceeds the size of the anomalies the enhanced structure is removed and leaving the background values. Note that the window size may not exceed the spatial variation of the background as I'(x,y) will deviate from the true background value. A window size of 11×11 pixels has been empirically found by this study to work for most tested steel plant

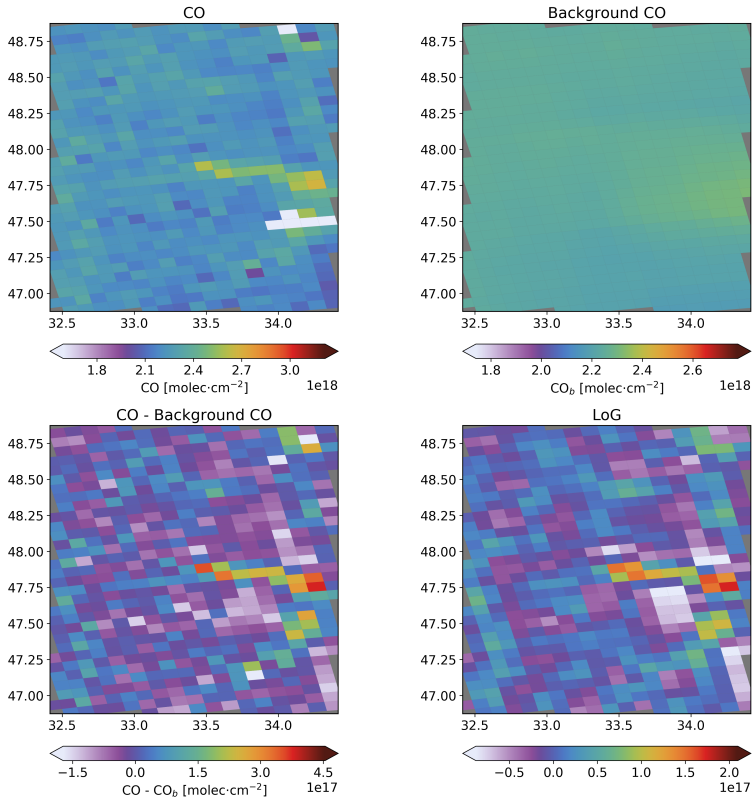

Figure 4.4: Pre-Processing applied on TROPOMI CO data to eliminate enhanced areas from the background. The example case shows the existence of a plume adjacent to the plume corresponding to the Steel Plant at Kryvyi (47.87°, 33.39°), Ukraine (6685.46).

cases. Once the background (I') is estimated, it is subtracted from the original image (I).

In the next step, convolution by a 2D Laplacian of Gaussian (LoG) filter is used to intensify rapid change in value. Prior to the filtering, the data has been linearly interpolated to fill missing pixels required for the convolution. Laplacian strengthens regions of local extremes by taking the second derivative of the image [Kong et al., 2013, Kumar et al., 2016, Vermeer et al., 2004]. In order to account for the high sensitivity to noise of the Laplacian convolution, the Laplacian was combined with a Gaussian smoothing filter; forming a Laplacian of Gaussian (LoG) filter (equation 4.2) [Kong et al., 2013]. The use of the LoG filter increases the contrast between the enhanced plume pixels and the bordering pixels (Figure 4.5). This is especially useful to ease the masking of a plume close to an adjacent plume as the contrast between the plume pixels and the space between the two plumes will be increased. This step is only done for masking and is not used for interpretation.

$$
\begin{aligned}
G(x,y;\sigma) &= \frac{1}{\sqrt{2\pi\sigma^2}} \exp\left(-\frac{x^2+y^2}{2\sigma^2}\right) \text{ (Gaussian)}, \\
\nabla^2 &= \frac{\partial^2 f}{\partial x^2} + \frac{\partial^2 f}{\partial y^2} \text{ (Laplacian)}, \\
\nabla^2 G(x,y) &= \frac{x^2+y^2-2\sigma^2}{\pi\sigma^4} \exp\left(-\frac{x^2+y^2}{2\sigma^2}\right) \text{ (LoG)}
\end{aligned}
\tag{4.2}
$$

In the second step the pixels are segmented into potential plume and background pixels. The Otsu algorithm is used to find a threshold that separates the strong enhanced potential plume pixels from the background pixels from the LoG image. Note that the pixels masked in the original CO image are not taken into account. Otsu is a threshold selection method that dichotomizes the pixels, into foreground and background, based on minimizing the intra-class variation of the gray scale histogram [Otsu, 1979]. The method is global threshold method, meaning that only pixel value information is taken into account leaving out information regarding spatial distribution [Dong, 2014]. Although its one-dimensional approach, Otsu thresholding is largely ap-

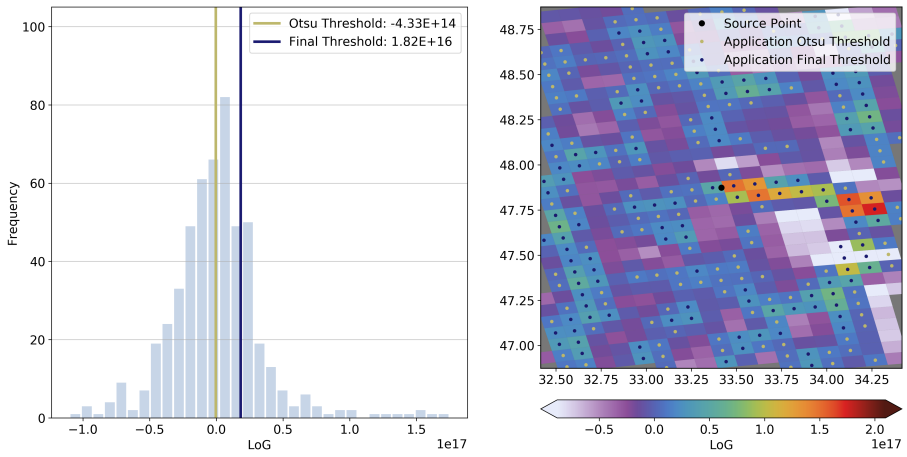

Figure 4.5: The thresholding algorithm is illustrated on the Bhilai plume. The first step consists of obtaining a threshold through the application of the Otsu algorithm on the LoG image with only taking the original un-masked into account. The median of the subset of pixels exceeding the Otsu threshold is used as the final threshold.

plicable due to its simplicity and robustness [Goh et al., 2018]. The true background is not homogenous due to fluctuating CO concentration. To separate the significant enhanced plume pixels from the 'higher' background values, the median of the thresholded foreground pixels is defined as new threshold. In equation 4.3, T stands for the global threshold value and A presents the set of pixels from image f(x,y) with a value greater or equal to T. The binary image g(x,y) results from thresholding f(x,y) using the median of A ($\tilde{A}$). Figure 4.5 illustrates the thresholding procedure.

$$A = \{f(x,y) : f(x,y) \geq T\}$$
$$g(x,y) = \begin{cases} 1 & f(x,y) \in A \wedge f(x,y) \geq \tilde{A} \\ 0 & f(x,y) < \tilde{A} \end{cases} \tag{4.3}$$

The potential plume pixels are indicated by the value "true" in the binary image. All connected potential plume pixels are assumed to belong to the same plume and a group specific integer value is assigned to all potential plume pixels. A connectivity of one is used, meaning that pixels connecting horizontally or vertically are considered connected. The image now consists of groups of potential plume pixels, each indicated by a unique value, and background pixels (labeled as 0 or "False"). The smallest distance, measured from projection point to center points, between the projection point and each group is obtained. Finally, the group closest to the projection point and meeting the set maximum distance of 14 km is assigned to the specific source.In addition, the assigned group may not originally consist of more than one third of originally masked pixels. The originally masked pixels do not contain information about the CO concentrations. As a result of the necessary interpolation prior to the LoG filter, originally masked pixels could be flagged as plume pixel after the thresholding. Plumes that have 'holes' will benefit from this, however for areas with a large number of masked pixels the true value and interpolated value could deviate strongly. Through trial and error of different set variables, we found that setting the threshold at one third seemed to both limit detection of false plumes and also limit discarding good plumes by allowing plumes to have originally masked data.

Once a specific plume pixel group is assigned to the source point, the plume mask image is obtained. The plume mask image is a binary image where the plume pixels and background pixels are indicated with, respectively, "True" and "False".

To account for holes in the plume due to masked data or weak local enhancement, morphological closing is performed on the binary image. Morphological operations concerns the processing of the image by the interaction with a structuring element. Closing comprises dilution prior to erosion of the image by the same structuring element, illustrated in figure 4.6. [Laganiere, 1998]. The used structuring element has square connectivity of one.

The final step of the plume detection algorithm includes the verification of significant enhancement of the assigned plume area among the surrounding pixels by the application of a student-t test. The student-t test

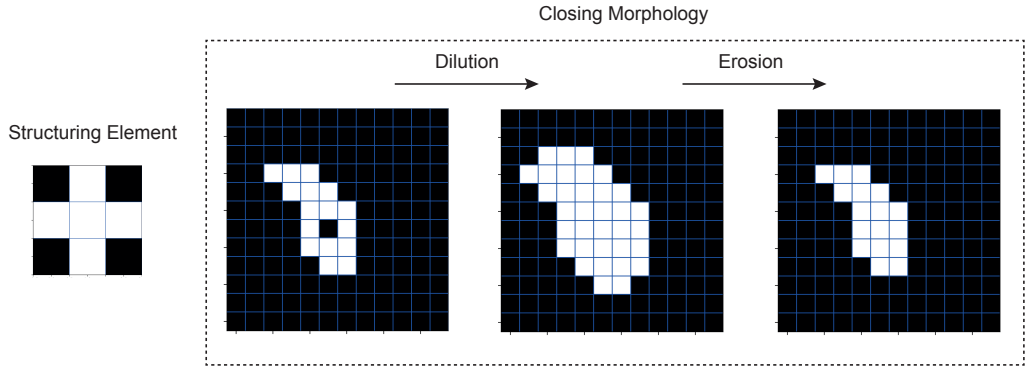

Figure 4.6: Closing morphology consists of dilution of the binary image by structuring element followed by erosion.

The earlier described Otsu method separates the image into two groups of pixels regardless of the presence of a striking intensified area. Thus, testing the significant difference of the obtained groups limits the false identification of background pixels as plumes. A confidence interval of 95% has been used.

4.2. Plume Center Line Identification

The second step in the framework consists of the identification of the plume center line. The extraction of the center line is necessary to in later steps compute the cross sections of the plume from (Section **??**) as well as the approximated plume direction. The center line is obtained using the earlier found plume mask (section 4.1). Using the plume mask, the natural slightly curved path of the plume is taken into account. Skeletonization of the binary image is performed to get a skeleton of unitary thickness centered within the original blob. The skeletonized image is a binary image, with the skeleton pixels being labeled as 1. The algorithm by Zhang and Suen iterates over the image, removing boundary and corner pixels while reserving the endpoints until only the skeleton remains. Details regarding the iteration process of the thinning method are found in Zhang and Suen [1984]. The skeleton serves as the base of the center line. Figure 4.9 presents the results of the steps followed for center line extraction.

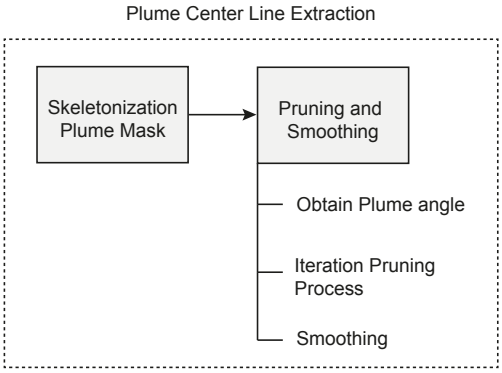

Figure 4.7: Overview of the process, consisting of two main steps, to extract the plume center line from the plume mask.

The extracted skeleton may contain side-branches besides the main branch as the result of either perturbation of the contour [Kruszynski et al., 2006, Saha et al., 2017] or falsely segmented pixels neighboring the plume. An obtained pruning method based on the discrepancy between the angle from one skeleton point to another and the main plume angle is applied. The main angle of the plume is determined by the median of the angles between the projection point and selected plume pixels weighted by their CO concentration. Prior to the calculation, the plume pixels are binned in groups based on their angle with the projection point

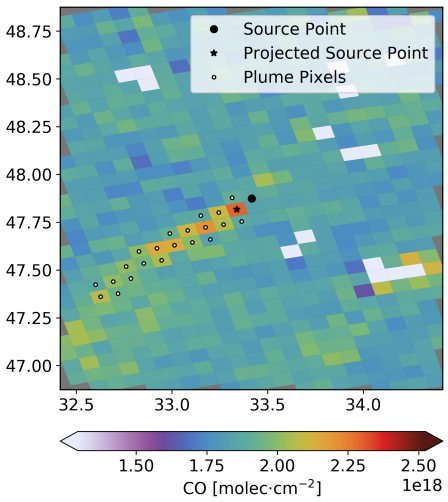

Figure 4.8: The starting point, or projection point, of the plume is estimated by the projection of the source point on the skeleton. The portrayed case, steel facility in Kryvy Rih (47.87°, 33.39°), Ukraine (01-08-2018), shows a distance between the source point and the identification of the plume.

where each group covered 30°. The pixels part of the group with the highest number of pixels are used to calculate the main angle from. The selection is necessary to increase robustness to multiple (or parts of) high concentration areas being identified as one.

Iterative transformations are applied to the skeletonized image following the points of the skeleton until an end-point is reached. Figures 4.10 and 4.11 present an overview of the pruning method decision scheme and the principle. The first iterative process starts at the determined starting point of the plume. The starting point is identified as the projection of the source point on the skeleton (see figure 4.8). The angle between the analyzed point and the neighboring skeleton pixels is determined, ignoring neighboring pixels analyzed in a preceding iteration. In the case of bifurcation, the neighboring pixel with the smallest difference in angle compared to the main plume angle is selected as part of the main branch. Skeleton pixels that are not part of the main branch are deleted. If the majority of the main branch pixels deviate strongly from the plume direction according to the main plume angle, the case is discharged. We defined the latter threshold as exceeding the empirically found value of 40° for more than half of the total skeleton pixels. The pruned skeleton is smoothed using spline interpolation. The small length of some plumes make that the lines only consist of limited (~5-15) coordinates. Therefore, the number of coordinates that define the line was increased prior to the interpolation. Increased information on the line in the form of coordinate points, improved the quality of smoothing.

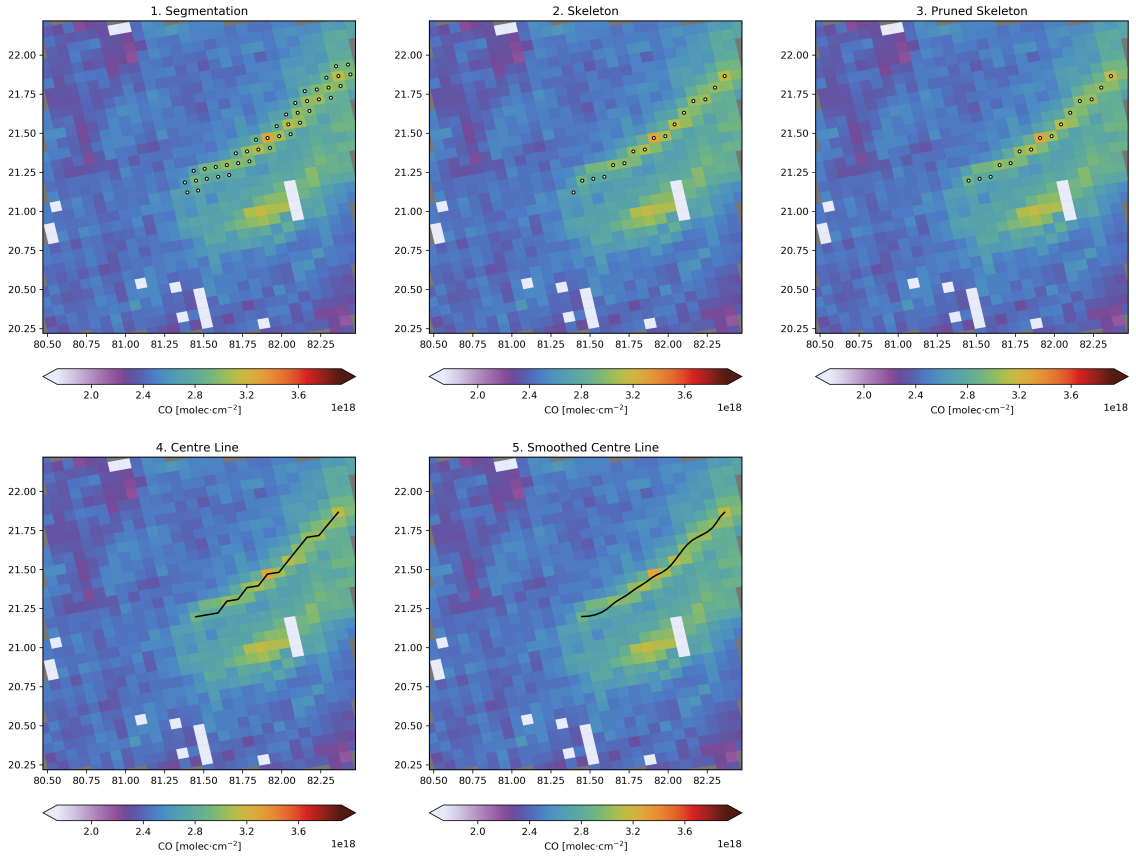

Figure 4.9: Processes to extract the center line of the segmented plume illustrated on the example of the Bhilai Steel Plant at 04-06-2019.

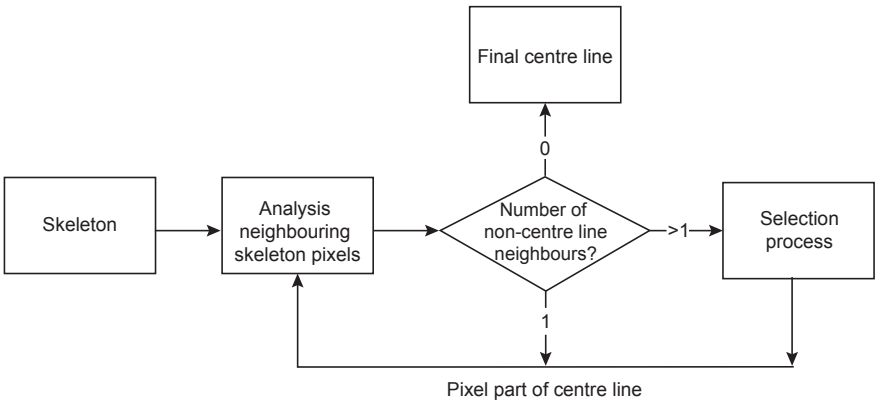

Figure 4.10: Decision scheme of the obtained skeleton pruning method.

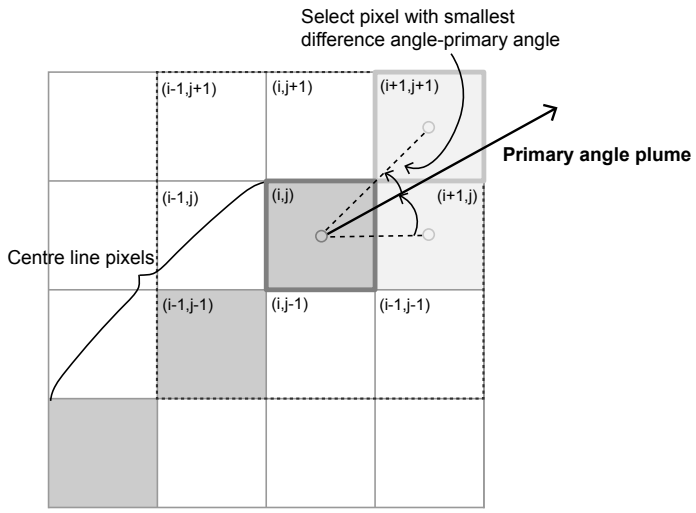

Figure 4.11: Selection of neighboring skeleton pixel in the case of bifurcation based on the angle between the centre pixel and each neighboring pixel in relation to the main angle of the plume.

4.3. Emission estimates: mass balance approach

The emission is estimated with the aid of the mass balance method on transection lines perpendicular to and following the extracted center line (described in section 4.2) in the downwind direction. Finally, the source rate of the plant is approximated by the mean value from the source rates of the different transects along the plume. The overview of the framework is shown in figure 4.12. First of all, the CO column data (X), with units in molecules/cm^2, is converted to the mass column (Ω), with units in kg/m^2. The conversion is done through multiplication by the molecular mass (M_{CO}) and the inverse of the Avogadro number (N_A) as shown in equation 4.4. The Avogadro number (representing number of units per mole) and molecular mass of CO are used to convert from the unit of number of molecules to the unit of mass.

$$\Omega = \frac{X \cdot M_{CO}}{N_A} \cdot 10^4 \tag{4.4}$$

To obtain the CO mass column value at the transection line locations, the irregular data is interpolated by performing triangulation.

The plume is assumed to be advection driven and thus the transportation of the plume is solely interpreted by the wind speed. The wind speed and the effective plume height are unknown. We interpret the wind speed by ERA5 re-analysis data at the single level of 100 meter. The wind speed is computed from the wind components using the Pythagorean Theorem. To allow collocation with the TROPOMI CO data at a specific location, we interpolated the ERA5 data. Due to the regular grid of the data, linear interpolation is used. Prior to the creation of the interpolation function, the computed wind speed data has been corrected to fit the observation time per pixel. The overpass time from the L2 TROPOMI CO data has been used and a linear relation over time was assumed. The wind direction is derived using trigonometric functions.

The rate through the cross-section at downwind distance x is obtained by the product of enhanced mass CO column ($\Delta\Omega$) and the wind speed (U):

$$Q = \int_{y_{l0}}^{y_{l1}} U(x,y)\Delta\Omega(x,y)\,dy \tag{4.5}$$

The source rate of the plant is approximated by the median value from the source rates of the different transects along the plume (see figure 4.12). The limits y_{l0} and y_{l1} (equation 4.5) refer to the boundary of the plume in the cross-wind direction. The concentrations at the limits are used to determine a reference for the background along the specific cross-section assuming a linear relation, illustrated in figure 4.13. The second background subtraction balances the background to zero to approach the true enhanced column value. The

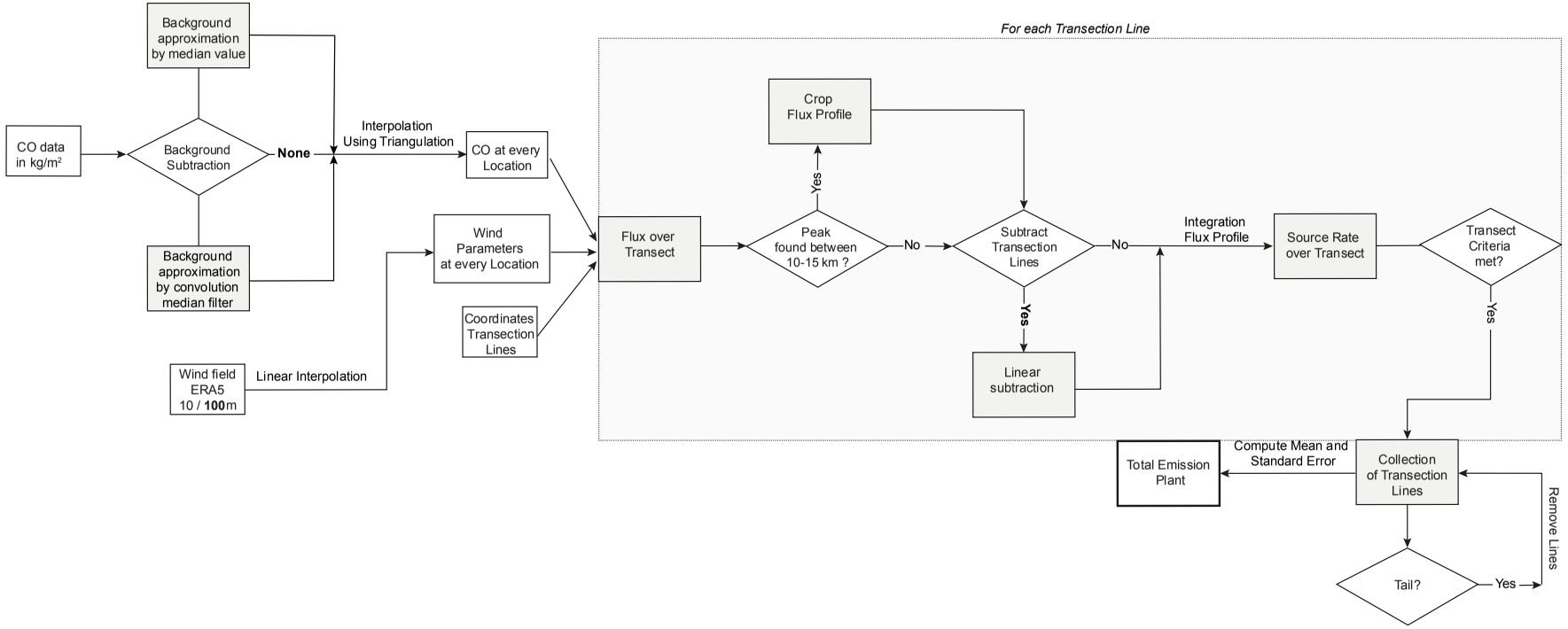

Figure 4.12: Overview of the processes and data used for the emission estimation using the mass balance approach.

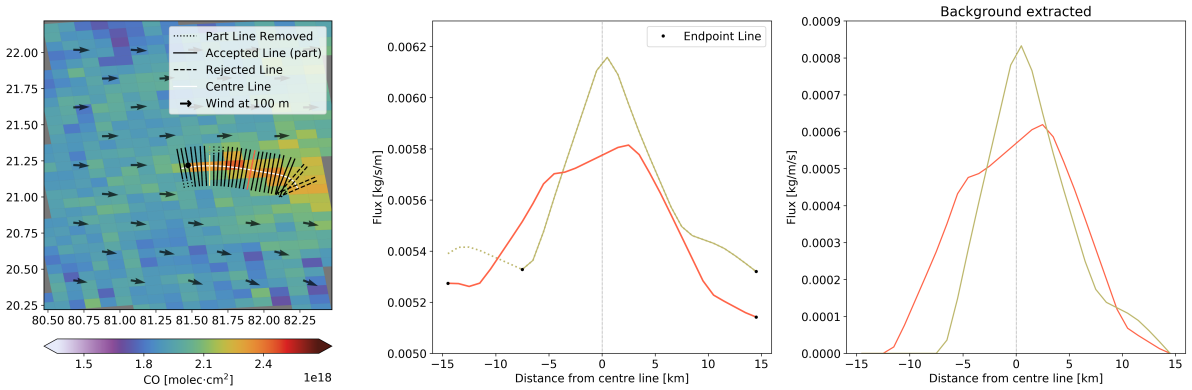

Figure 4.13: Calculation of the flux profile through transects perpendicular to the extracted plume centre lines. The dashed transection lines are rejected due to deflection in direction in comparison to the wind direction (indicated by the black arrows). The dotted line parts indicate cropping of the fixed transection line width due to the occurrence of a through in the flux profile (indicated by a black dot in the flux profile). As an example the flux profiles, before and after background subtraction, of a cropped and non-cropped transect are delineated, respectively, in yellow and red lineation. The case illustrated concerns the Bhilai Steel Plant (BSP), India, at 16/06/2018.

transition of background to plume, and vice versa, is identified by locating the throughs in the transection profile. The transection line is initially fixed at an empirical found width of 30 km by this study. Significant throughs occurring from ± 5 km, seen from the centre point, are identified as transition point. If no negative peaks are found, the limits are set at -15 and +15 km in the cross-wind direction from the centre point. The detection of negative peaks is especially important for limiting potential emission overestimation or underestimation caused by higher concentrations from adjacent sources.

To assure the quality of the estimated source rate from the integrated fluxes through the transects, the transection lines taken into account will be selected. To verify the use of the wind field at 100 m height, the discrepancy between the wind direction from the interpolated ERA5 data set and the direction indicated from the extracted plume centre line serves as criteria. The transection line is discarded when the difference between the wind and plume angle comprises 30°. Figure 4.13 presents the rejection of transection lines due to exceeding the set threshold indicated by dashed lines. Furthermore, the analogy of the maximum flux and the centre point of the transection line act as a proxy of the transection line quality. The segmentation and extraction of the centre line do not necessary limit the coverage of the plume to the high enhanced values of the plume. Taking into account emission rates determined from transection lines covering transition values might lead to an emission underestimation. In ideal cases the extent of the plume can be identified in the downwind emission profile by the presence of a plateau-shaped feature. The fanning of plume values is identified as a 'tail' like feature with emissions significantly lower than the plateau. The tail is characterized as the occurrence of a significant large amount of points (more than one-third of the total) below the median of the downwind emission profile as presented in figure 4.14.

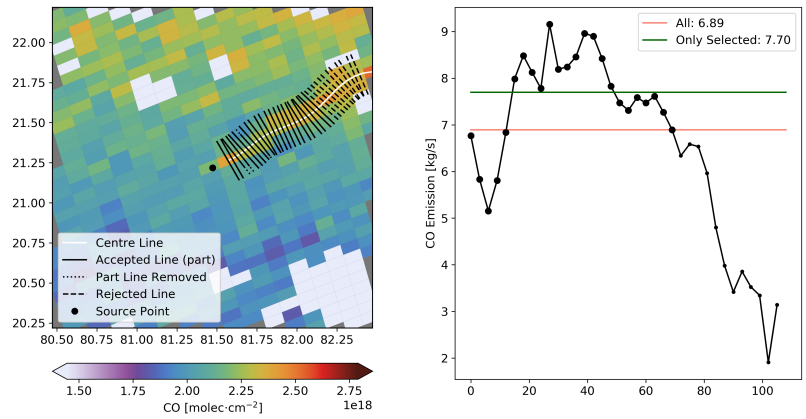

Figure 4.14: Example of segmented plume (BSP, India ,24-06-2018) containing a significant amount of points at the end of the plume that do not correspond to the enhanced plume values. The so-called 'tail' transects are deselected (indicated by the dashed lines). The downwind emission profile illustrates the difference between taking into account all transects and only taking into account the selected transection lines. Inclusion of the lower emission will result in a lower total emission depending on the value and number of 'tail' transects.

4.4. Filtering

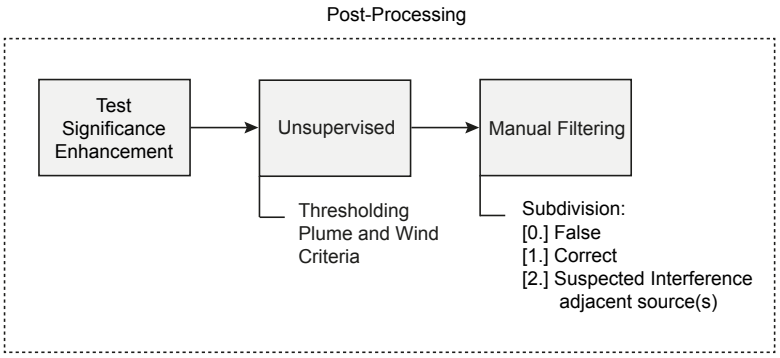

Figure 4.15: The detected plumes are validated over two steps. First of all, the plume enhancement must exceed the variation occurring in the background. The limit is derived from the collection of standard deviations of the surrounding pixels covering all processed orbits. The post-processing consists of an unsupervised and manual filtering step.

To test the occurrence of the detected plume area to a significant release of CO into the atmosphere from the specific point source, a signal threshold is set. The threshold is defined as the boundary distinguishing background variability and enhancement declared as a positive CO surface flux. If the enhancement of the plume surpasses the threshold, the detected plume area is accepted. The plume enhancement is determined by the median value of the maximum CO concentrations over each line transect. The threshold is set as the upper limit, using bootstrapping with a confidence interval of 97.5%, of the standard deviation of the surrounding pixels over the entire time series. For each location a new threshold is computed to account for the strong deviation of accumulated CO spatially (Figure 4.16). Besides the spatial variation of the CO background, a seasonal variation is clearly visible. However, the set threshold remains constant over time to limit uncertainty caused by the temporal irregularity of the data. Notice that the obtained threshold could overestimate the true variability of the background if the majority of the considered data contains signals of multiple plumes.

The unsupervised post-processing step consists of application of several thresholds to secure desired criteria concerning the following:

- Correspondence plume and wind direction

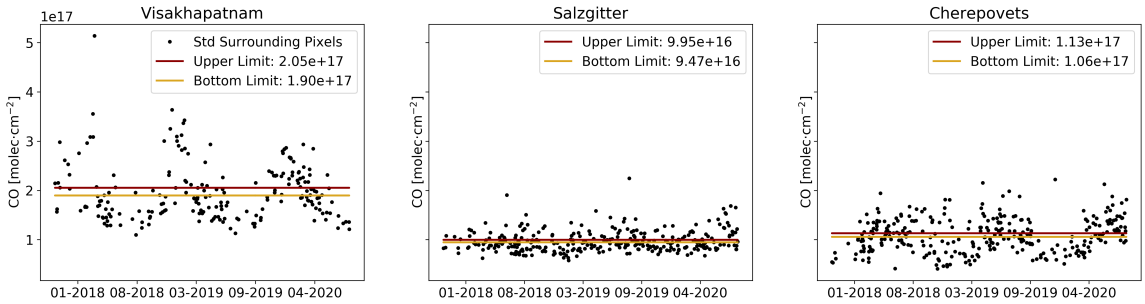

Figure 4.16: Time series of the standard deviation of CO signals from surrounding pixels, all pixels not identified as the plume corresponding to the source point, of the (left) Visakhapatnam, (centre) Salzgitter and (right) Cherepovets steel plant. The upper and lower limit represent the confidence intervals at 2.5 and 97.5% ,respectively, obtained through bootstrapping.

- Flux profile over each transect
- Wind conditions
- Variation Emission profile in the downwind direction
- Number of selected transection lines to interpret the emission from

The selection of thresholds for the specific criteria were mainly empirically obtained. Several locations, using the entire time series, were used as test cases (e.g. Bhilai, Kryvyi Rih, Rourkela, Duisburg, Vanderbijlpark, Cherepovets, Lipetsk, etc.) to determine and optimize the selection of criteria and their thresholds. An iterative manual trial and error approach was used.

Similar to the procedure used for the selection of the transection lines, the discrepancy between the plume and wind field angle as well as the deviation of the flux peak along the transects are used as criteria. The median value of the properties covering the collection of selected plume transects should not exceed the threshold, rather than the focus on individual lines during the procedure described in section 4.3. The empirically obtained thresholds for the difference among the obtained plume directions and location of the flux maximum among the plume cross-sections are set, respectively, at 20° and 6 km. The combination of looser and stricter thresholds for individual transection lines and the overal plume (represented as the collection of selected transects) optimize the detection of proper cases. As can be seen in figure 4.19, the proxy for the quality of the defined plume centre line successfully discards cases with a misplaced centre line.

To confirm the application of the mass balance approach, as previously described in more detail in section 2, the wind field should be more or less homogenous and not consist of low wind speeds. We define the largest difference in wind angles found along the centre line as proxy for the homogeneity of the wind field. We empirically determined the homogeneity threshold and it was defined at 10°. Figures 4.17 and 4.18 present discarded cases due to the exceeding of the wind fit and wind variation criteria respectively.

Although the emission over the extent of the plume will vary due to fanning, a major variation could indicate false detection. The coefficient of variation (CV), standard deviation (σ) relative to the mean ($\overline{X}$) (see equation 4.6), is used to define the variation of the emission over the plume extent. A large variation of estimated flow rates over the plume could. We empirically set CV at a ratio of 0.4 since it appeared to set fit the balance best for respecting the natural variation of the emission profile (fanning out will cause lower values) and filtering bad cases. Note that the set value of CV is critical for the balance between limitation of false detected plumes and optimizing the detection of true plumes. It is advised to revise the variation threshold when the framework is applied on different cases.

$$CV = \frac{\sigma}{\overline{X}} \tag{4.6}$$

In order to verify and assure the quality of the source point's emission rate estimation from the emissions interpreted over each transects, a minimum number of transection lines (6) was set as a requirement.

A manual filtering step is applied to verify the quality of the obtained emissions of the remaining cases after the post-processing step. The quality of the emissions estimated from each overpass is assessed through inspection of the located plume centre line and the transects among the mapped CO signals. Through the

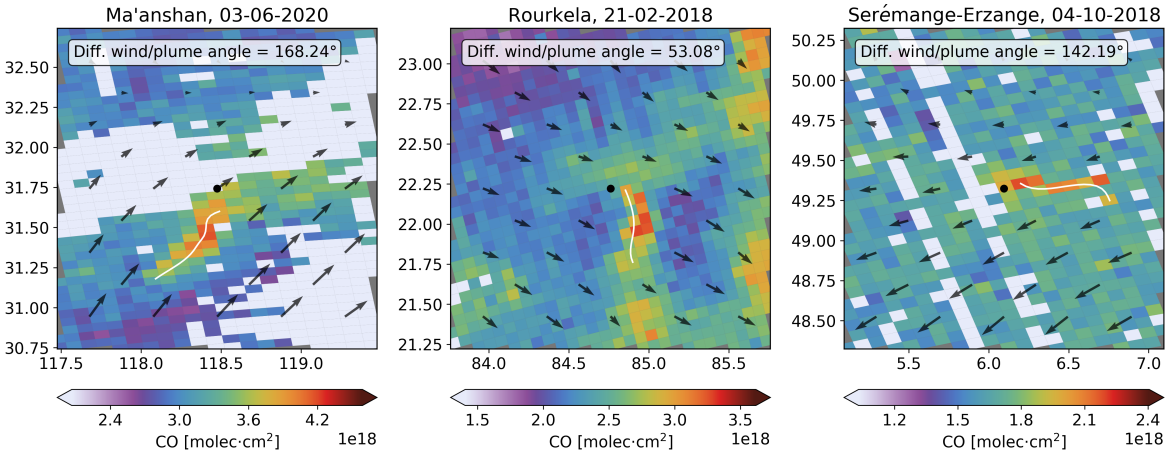

Figure 4.17: Examples of cases discarded due to major discrepancy between the wind direction and the plume direction obtained from the extracted plume centre line.

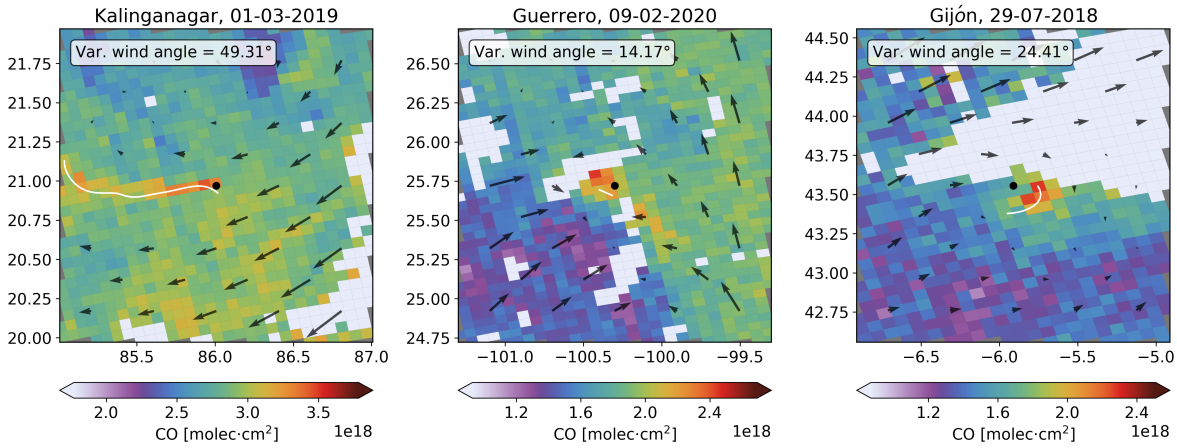

Figure 4.18: Examples of cases discarded due to large variation of the wind direction over the plume area and thus nonuniform advection.

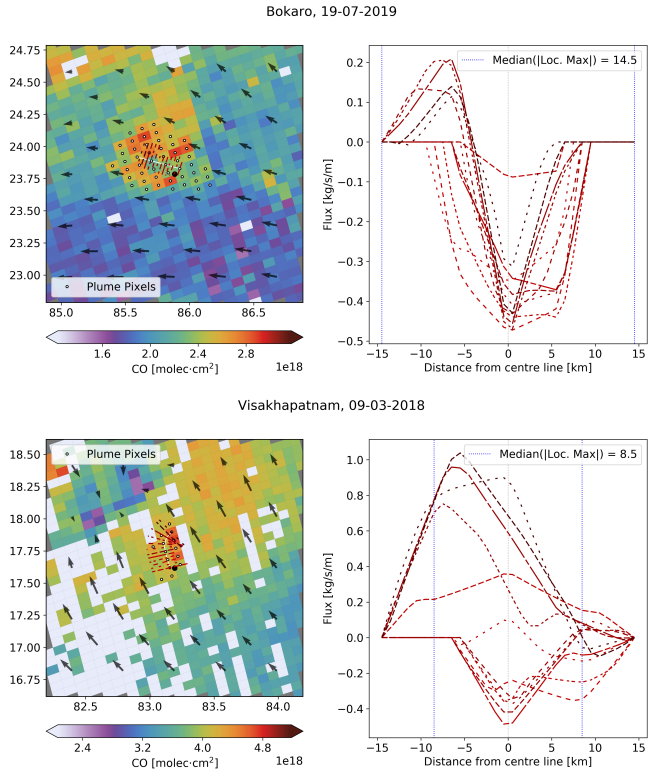

Figure 4.19: Rejected plumes based on exceeding the allowed deviation of the flux peak from the centre line. The criteria aims at detecting mis-located centre lines, such as in the Bokaro (19-07-2019) plume, caused by the covering of two plumes by the plume mask , and the Visakhapatnam (09-03-2018) plume.

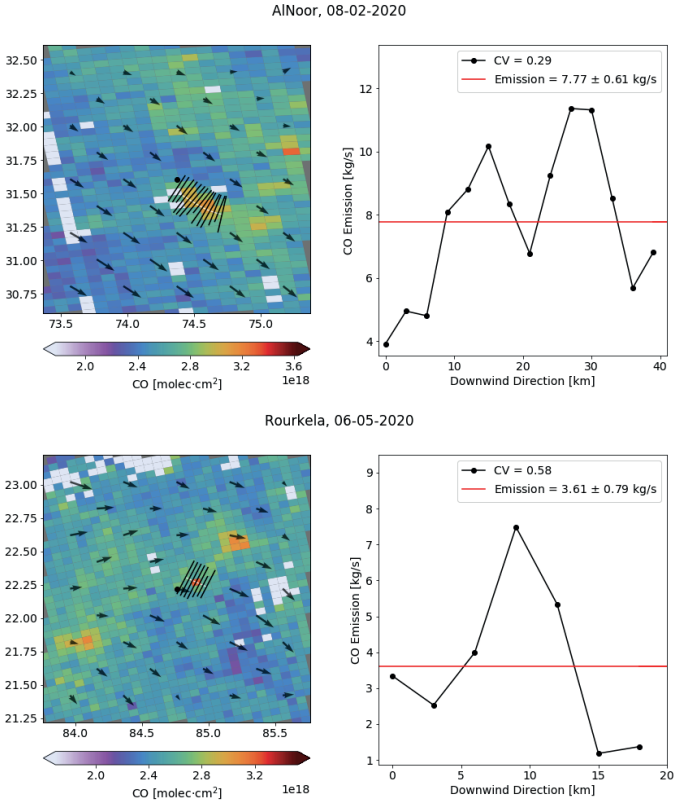

Figure 4.20: Examples of cases, AlNoor (08-02-2020) and Rourkela (06-05-2020), respectively, meeting and exceeding the criteria set for the emission variation among the downwind direction. The variation is defined as the coefficient of variation (CV). A single enhanced pixel caused the false detection of the plume at Rourkela.

manual filtering, the detected plumes are divided over three groups by labeling each case with one of the following flag values:

0. False detected plume or poor quality
1. Good quality
2. True detected plume with suspicion of interference of one or multiple nearby plumes

Plumes flagged as 0 will be eliminated from the dataset used as input for time series analysis. Figure 4.21 illustrates examples of frequent cases labeled with flag values 0, 1 and 2.

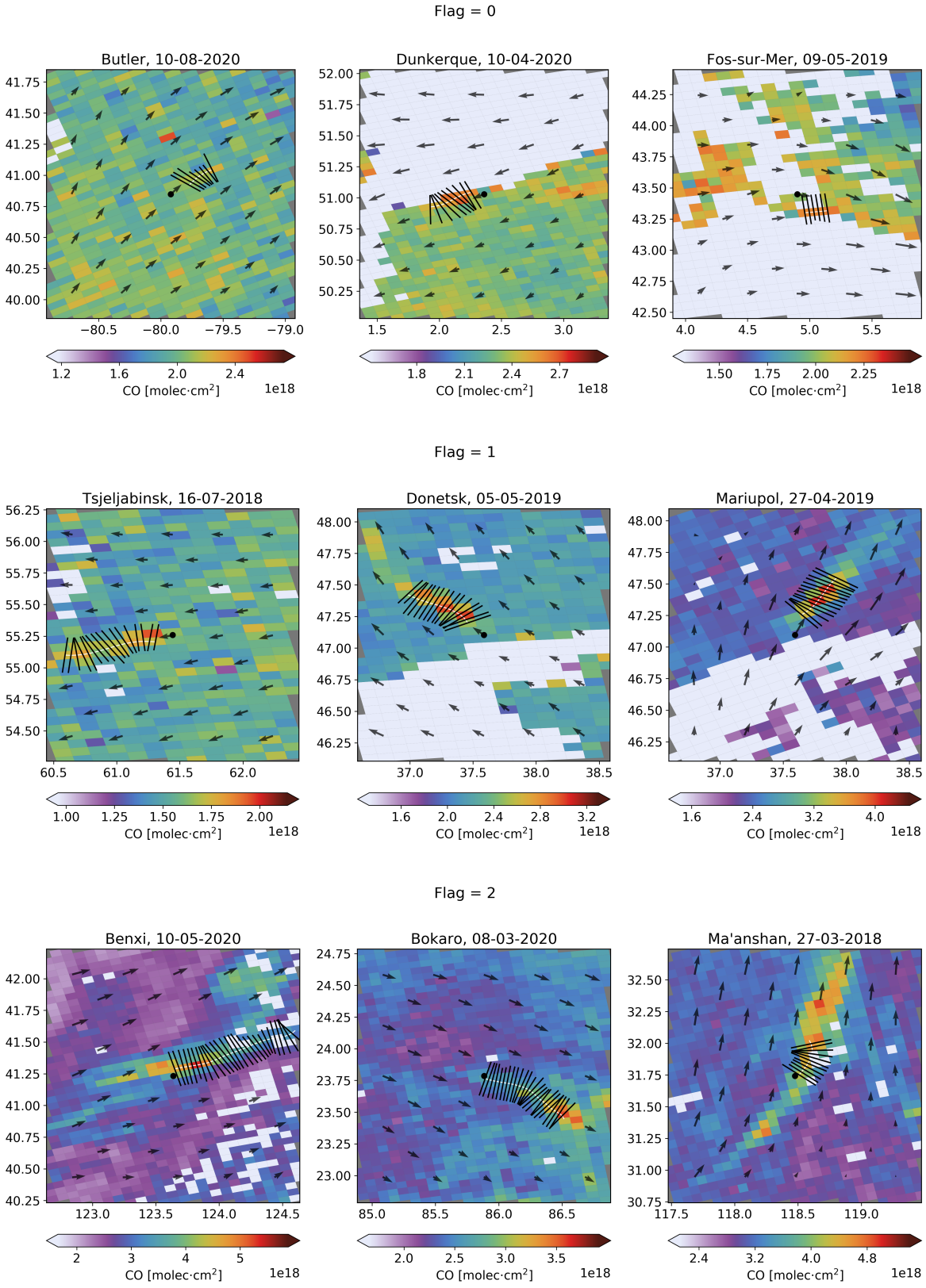

Figure 4.21: Examples of cases manually labeled as 0, 1 and 2. Plumes are flagged as 0 if, e.g., a plume is falsely detected (Butler, left), the quality of the plume is poor (Dunkerque, centre) or a potential plume could not be properly identified (Fos-sur-Mer, right) due to the presence of an excessive number of masked pixels. The middle row presents examples of correct identified plumes. The emissions of plumes flagged as 2 are potentially influenced by other plumes from nearby sources. This could be seen through visual inspection, as the alignment of two plumes as in the Benxi (left) or Ma'anshan (right) plume causing accumulation of CO or as the capturing of multiple plumes due to failed identification of the plume path (Bokaro, centre).

4.5. Performance Quality of Algorithm

To filter false detected plumes and plumes not meeting the requirements, the significance of the plume enhancement was tested whereafter post-processing, unsupervised filtering followed by manual filtering, was applied. Where the requirements set for desired plumes emerged from the assumptions made for the application of the mass balance approach. Figures 4.22, 4.23, 4.24 and 4.25 illustrate the results and performance of the filtering processes. The overview in figure 4.22 presents the results of the entire dataset. The figure reveals the rejection of measurements obtained by the main part (segmentation, line extraction and emission estimation) of the framework through the enhancement testing and post-processing steps. From all measurements, only 5.8% was ultimately accepted. The ratio of plumes meeting the minimum enhancement criteria found for all plumes (60%), figure 4.22, corresponds with the ratio's found per individual steel plant (58.4±1.4 %). The consistency in the ratio, for most steel plants, can be seen in figure 4.23. Furthermore, the strong correlation between geographical location and number of cases, as was noticed in figure 3.6, appeared to be less apparent in the results of the first filtering process. From the three filtering steps, the unsupervised post-processing step discards the most cases with an average acceptance rate per plant of 9.7±0.8% and 12% acceptance rate of the measurements from significantly enhanced plumes.

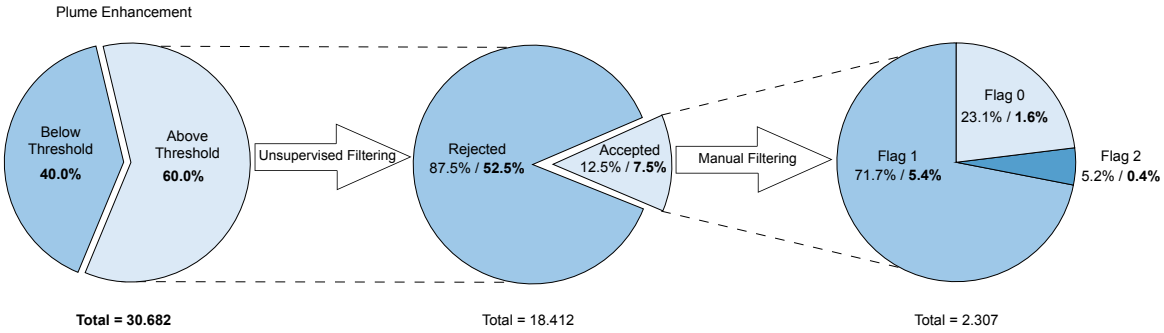

Figure 4.22: Overview of the results from the three filtering processes: plume enhancement test, unsupervised post-processing and manual post-processing. The bold percentages refer to the number of measurements in the sub-group relative to the total measurements used as input for the filtering process (output detection algorithm)

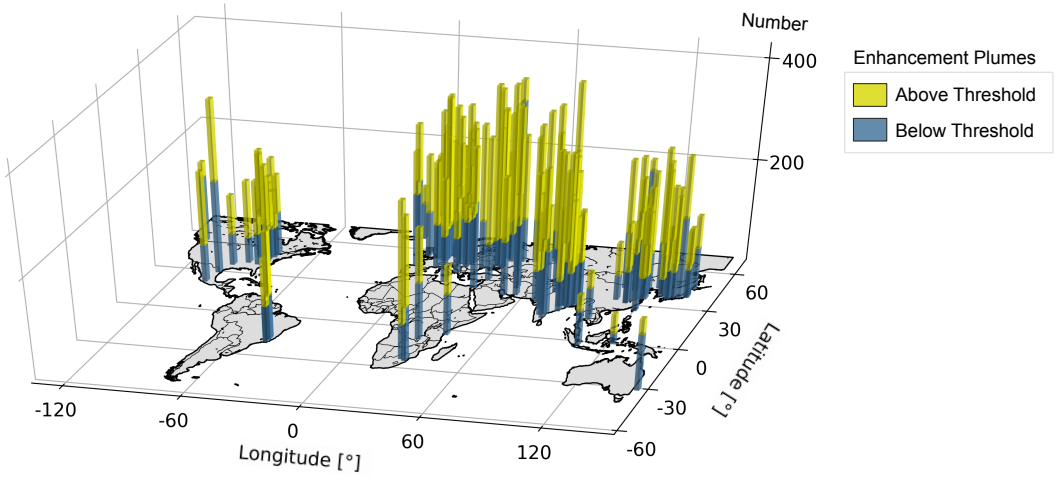

Figure 4.23: Number of discarded (bottom, light blue) and accepted (top,yellow) emission estimations by the enhancement test, the first filtering process. The total stack height for each facility represents the total number of measurements processed by the detection algorithm.

The unsupervised filtering was, besides limiting false detection, designed to discard plumes that did not meet the assumptions made in the mass-balance approach (e.g. uniform advection, no low wind speeds). The number of plumes not meeting any or multiple of the six criteria can be seen in figure 4.24, with the

red lines indicating the occurrence of discarded cases solely based on not meeting the specific criteria. The majority of the discarded plumes did not meet the criteria regarding the required analogy between the wind and plume direction. Over 18% of the discarded plumes, were solely discarded based on this criteria. Besides the verification of the use of the 100 meter wind field, the agreement between the wind field and plume angle appeared to be of great importance for identifying false detected plumes. Insight into whether a discarded case was a not desired detected plume or false detected plume appeared difficult to obtain without visual inspection.

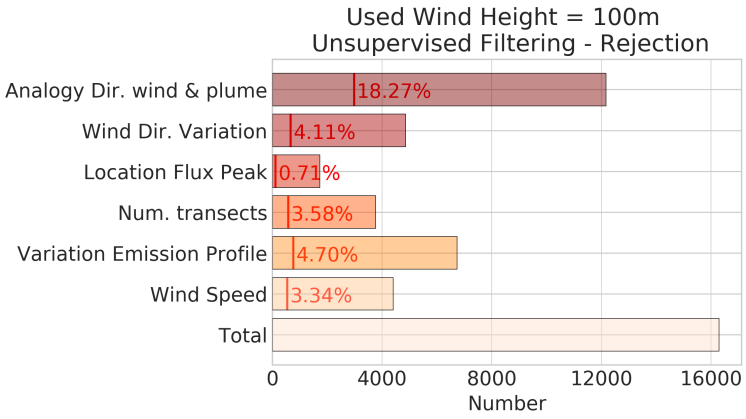

Figure 4.24: Insight into the number of measurements not meeting the requirements for each criteria set for the unsupervised post-processing step.

After the unsupervised step, the remaining detected plumes were verified through visually inspection. Measurements indicated with flag 1 (good plume) or 2 (true detected plume but with possible interference) were accepted as true plumes, respectively, 5.4 and 0.4 % of the total measurements. We found that the amount of measurements rejected through manually filtering, deviated strongly per facility. Figure 4.25 shows the distribution of the accepted and rejected, through unsupervised and manual filtering, for steel facilities in Europe. From the figure, it was noted that for the steel plants located in coastal area's, e.g. the Netherlands, France, Belgium, UK and Spain, relatively a large amount of measurements were rejected through manual filtering. The occurrence of masked plumes near coastal area's increases due to the inability to retrieve measurements above clear-sky waterbodies (not enough light is received to fulfill the retrieval). Furthermore, it was found that most rejected measurements corresponded to facilities with a small number of measurements (see figure 4.26). The rejection of measurements from plants with over 60 remaining measurements after the unsupervised filtering accounts for only 10.5% of the total elimination through the manual filtering step. However, 76.2% of the rejected measurements correspond to plants with less than 40 emission estimations over time with the accepted measurements consisting of measurements flagged as 1 (true detected plume) or 2 (true detected plume but with suspicion of interfering signal from adjacent plumes). The distribution of the number of accepted measurements, for both only taking into account measurements flagged as 1 and all true detected for all steel facilities is presented in figure 5.2.

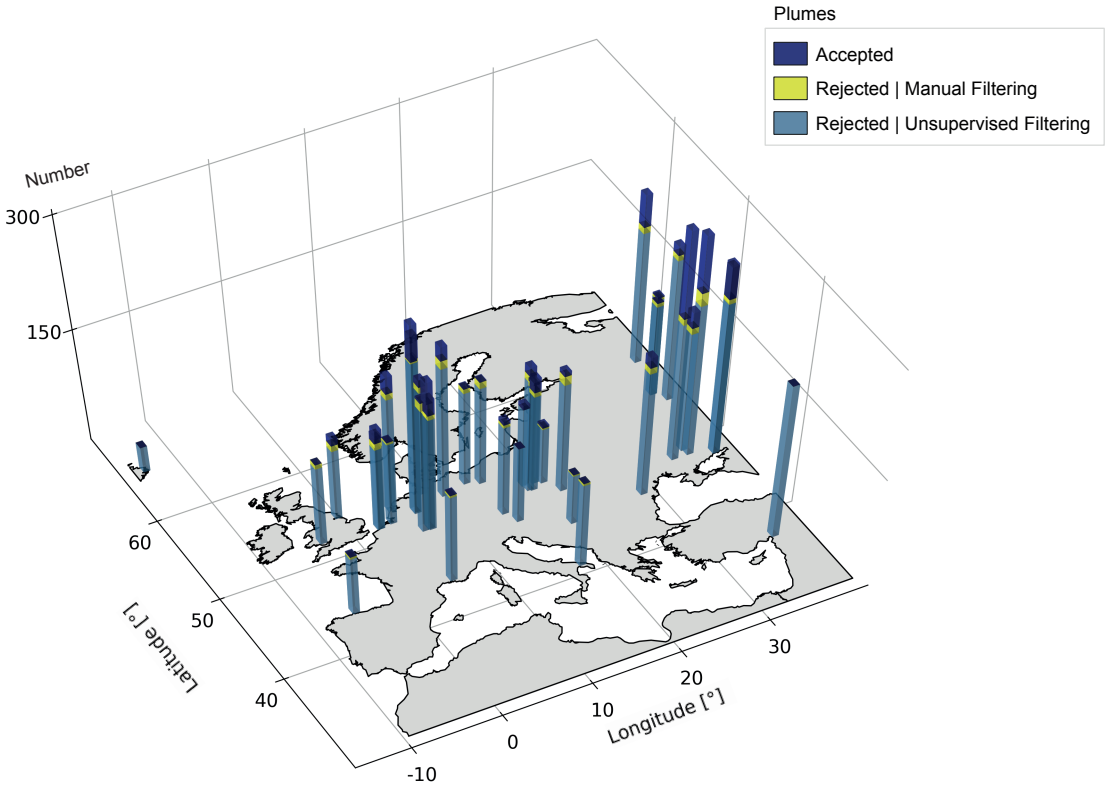

Figure 4.25: Number of discarded plumes by the post-processing steps, unsupervised (bottom, light blue) and manual filtering (centre, yellow), and accepted (top, dark blue) cases from in Europe located steel plants.

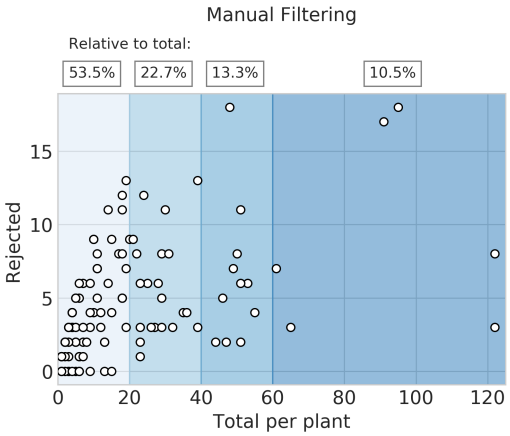

Figure 4.26: Relation between the number of rejected measurements and the number of total measurements per steel plant. The blue fillings separate the points based on the number of total of measurements (num): num≤20,20<num≤40,40<num≤60 and num>60. The percentages above the plot indicate the number of rejected measurements per group relative to the total rejected measurements (of all steel plants) through the manual filtering process.

5. Results

5.1. Time Series and Validation

The characteristics of the individual time series differ on facility level. In figure 5.1 a representative collection of carbon monoxide emission estimations obtained with the framework is shown for 8 facilities over the time period of mid November 2017 to mid August 2020. The number of CO measurements per plant varied between 0 and 119, where the majority of the series consisted of 10 estimations (Figure 5.2). Table 6.1 presents all listed steel plants facilities including the found number of estimates and the average emission. The emissions measured vary over steel plants from ~2.5 up to over 40 kg/s. From Figure 5.2 it can be seen that the scattering of measured emissions changes per plant. In some time series apparent groups of clustered emission values are present.

On plant level the distribution of measurements over time is not constant. Long gaps of up to multiple months alternate with periods of more frequent subsequent measurements as visible in Rourkela, India and Dabrowa Gornizca, Poland. Not all outliers corresponded with measurements possible interfered by adjacent sources (indicated by the red bullets in Figure 5.1).

Validation of the necessary, especially with the found fluctuations of emissions measured. The correlation between European Pollutant Release and Transfer Register (E-PRTR) data and emission estimations obtained through the framework was tested. To compare our data with the E-PRTR data which is provided in tonnes per year, we transformed the data to kg/s by assuming a constant emission [Mortier, 2020]. The analysis was limited to facilities of whom information regarding the CO emissions was found in registers and had at least 15 measurements over the obtained time series. Although this study collected information on facilities using another accessible inventory, the National Emissions Inventory (NEI) from the United States Environmental Protection Agency (EPA), no representative amount of emission estimations of the corresponding plants were obtained. A Pearson coefficient of 0.76 found for the correlation between E-PRTR data and the framework results. Furthermore, it should be noted that our measurements had a higher emissions than registered in the E-PRTR. Given that our comparison was done on a limited number of facilities, care should be taken with drawing conclusions.

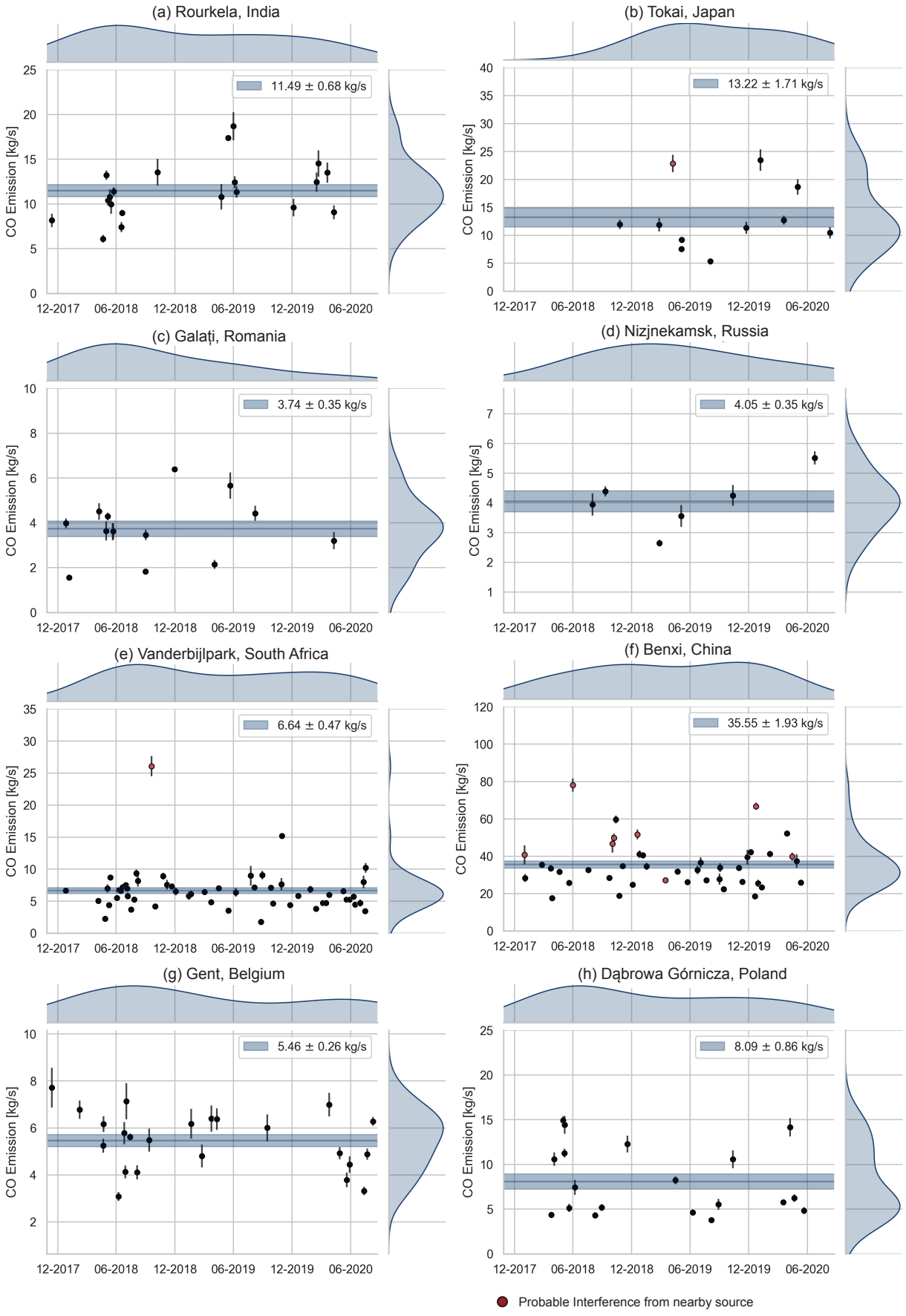

Figure 5.1: Collection of 8 time series representing CO emission estimates obtained using the proposed framework over a time period of mid-November 2017 until mid-August 2020. The shaded area indicates the mean and standard error of the measurements.

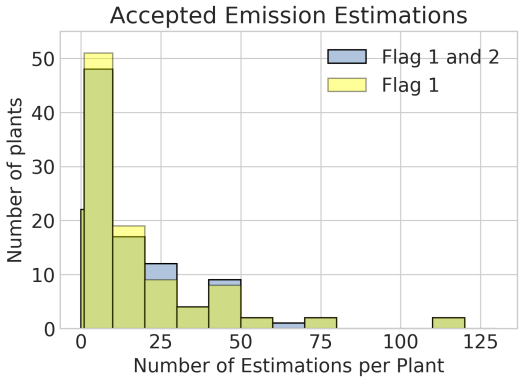

Figure 5.2: Histogram presenting the distribution of the total emission estimations, taking into account all true cases (blue, flag 1 and 2) or only the high quality cases (yellow, flag 1), obtained over a period of more than 2.5 years for 133 steel plants.

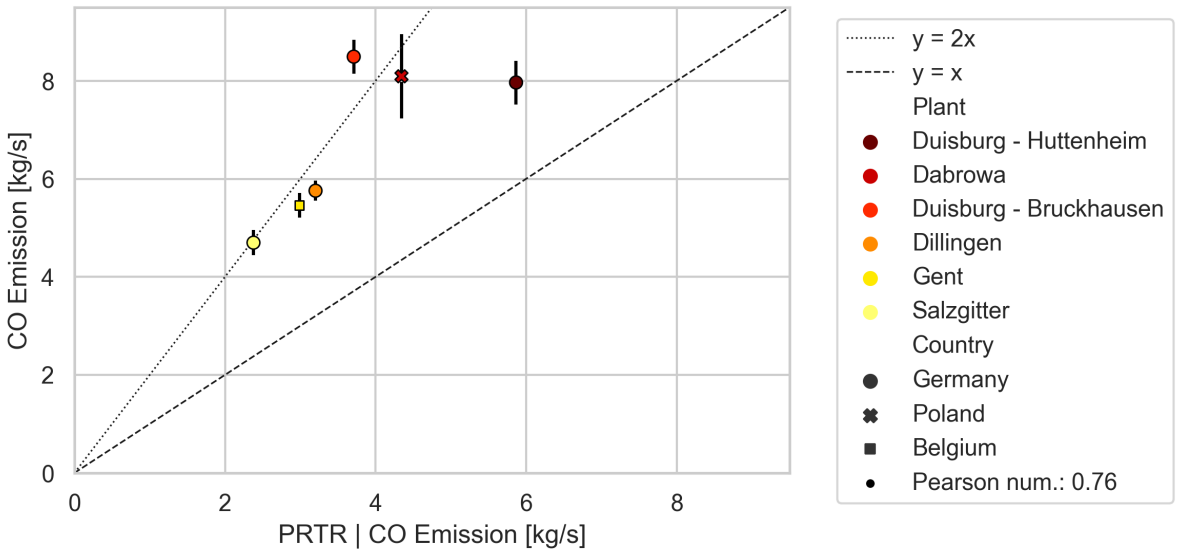

Figure 5.3: Relation between the emission rates estimated by this study and the emission rates documented by facilities in the E-PRTR. Only steel plants with 15 measurements are presented. The x-axis and y-axis respectively, represent the value of the plant as registered in the E-PRTR and the average estimated emissions over time. The error bars indicate the standardized error from the obtained emission estimations per steel plant by this study. Note that the PRTR rates are obtained from an annual emission value by assuming a constant emission rate.

5.2. Uncertainty

The developed framework was used to determine emission estimation uncertainties through testing of different variable settings. The potential biases from the used background extraction method, to obtain only the enhanced plume concentration, and the selected effective wind height were examined. The analyses were done through comparing the results obtained using different settings with the results obtained using the setting as initiated in framework (here referred to as the 'reference'). First of all, no correlation (Pearson coefficients ~0) was found between the estimated emissions using the proposed framework settings and CO background variation. Figure 5.4 presents the examination for two steel facilities located in Tsjeljabinsk and Lipetsk.

No striking difference between the emissions obtained using our 'reference' settings and the alternative background extraction methods was found (Figure 5.5). The alternative methods made use of the extraction of an overal estimated background as done in the plume elimination step described in Section 4.1 or approximated by the median value of background pixels. The relative comparison for each alternative method with the reference case showed only small variation over different steel plants (bottom graph in Figure 5.5). Over all steel plants the average relative value was found to be 98.20±0.49%.

A significant bias was found for the wind height. Both subsets, wind field at 10 and 100 meter (reference case), from the ERA-5 reanalysis data were used. Higher emissions were found for the use of the (higher velocity) 100 meter wind field (Figure 5.6). Interestingly, the number measurements rejected

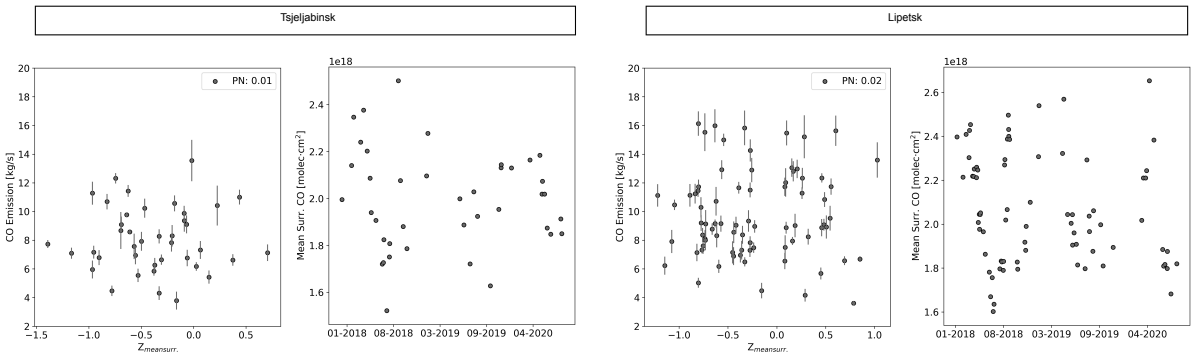

Figure 5.4: On the left (for each case), correlation between the standardized surrounding pixels (non-plume) and emission estimation interpreted from the plume. On the right, the mean of the surrounding pixels of the total 1°×1° over time. PN refers to the Pearson Number between the standardized concentration of the surrounding and the estimation CO emissions.

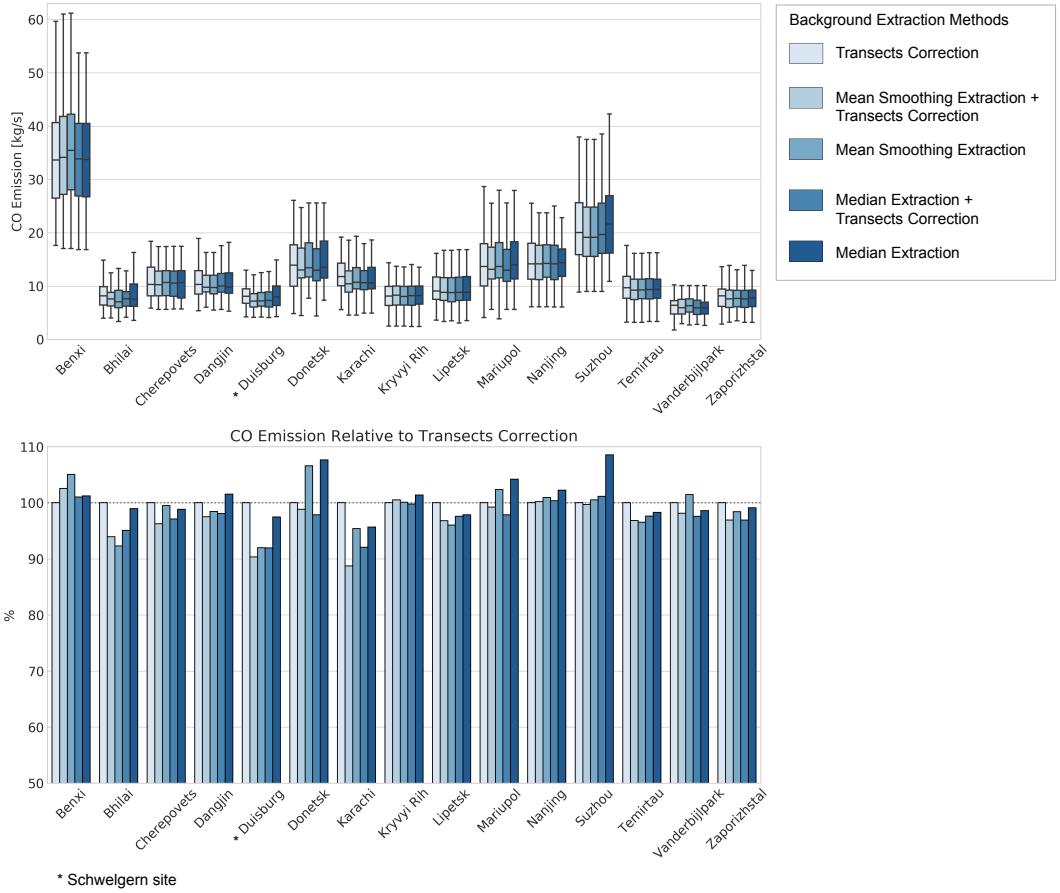

Figure 5.5: Results of running the framework for several steel plant locations using different background extraction techniques applied during the emission estimation step. The used techniques concern no overall background extraction from the CO columns, overall background approximated by mean smoothing filter and overall background approximated by the median of the non-plume pixels. The techniques are combined with a background extraction only applied at each transects or only the overall background extraction method is used. We refer to the measurement resulted from the run using the 'Transects Correction' method (method applied in this study) as the 'reference measurements'. The bottom graph presents the results relatively to the 'reference' measurements. The steel plants listed all have 40 or more measurements for all runs. The Duisburg facility concerns the Bruckhausen plant.

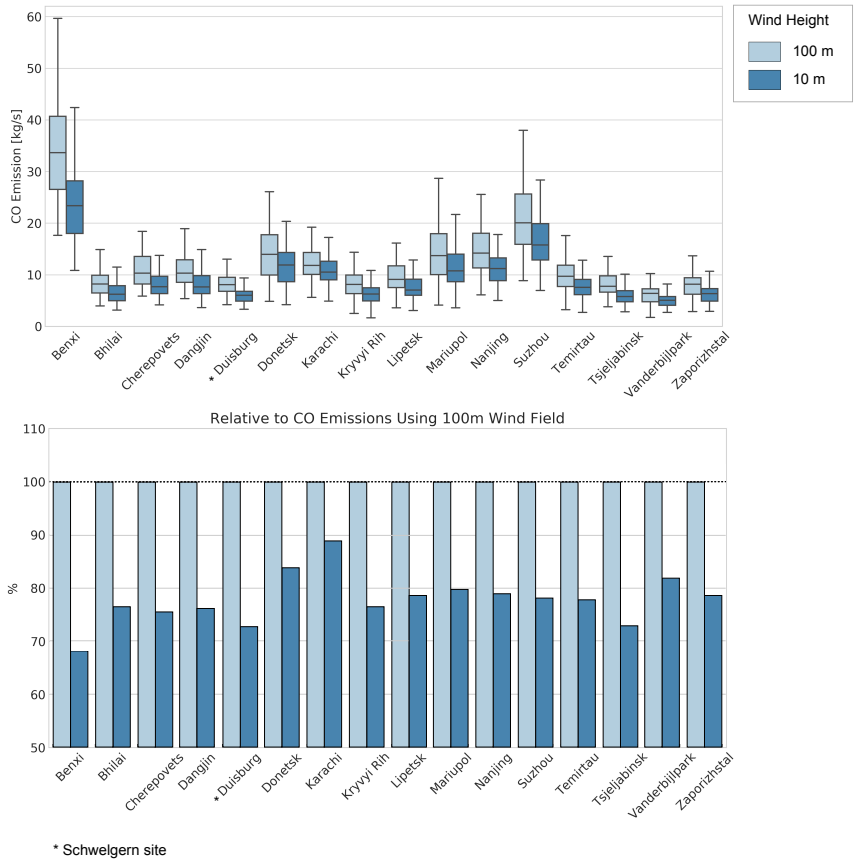

Figure 5.6: Results of running the framework for several steel plant locations using the wind profiles from 10 and 100 meter. We refer to the measurement resulted from the run using the 100 meter wind (used in this study) as the 'reference measurements'. The bottom graph presents the results relatively to the 'reference' measurements. The steel plants listed all have 40 or more measurements for all runs. The Duisburg facility concerns the Bruckhausen plant.

5.3. Data interpretation and analyses

The applicability of the obtained emission estimates to detect change over time was tested. Care should be taken with the interpretation of perceived emission deviation. Steel plants are often accompanied by nearby carbon monoxide emitting sources that could potentially affect the measurements. Therefore, we started with the interpretation of emission measurements over time. The analyses were done using the measurements from the Bhilai Steel Plant (India) and the ThyssenKrupp steel works Huttenheim and Schwelgern located in the Duisburg area (Germany). The Bhilai plant is surrounded by multiple steel processing facilities as well as cement plants (Figure 5.7). Correspondence was found, through visual inspection, between clear CO enhancements (plumes) and the location of steel facilities and a pelletization plant (indicated by A and B in Figure 5.7) in the North-East direction from Bhilai (e.g. images A, C and D in Figure 5.11). The distance between the facility located in Bhilai and the apparent large CO emitting source or sources (from A/B) totals roughly 35 km. Higher density of sources were found in the surrounding area of Duisburg. ThyssenKrupp's Huttenheim and Schwelgern sites, roughly 18 km apart, are the largest CO emitters in the area according to E-PRTR (Table 5.1).

The obtained time series of the Bhilai facility, Huttenheim and Schwelgern site showed alternation of emission value. The measurements were clustered using Kmeans on plant base to ease visual interpretation and inspection of the occurrence of higher and lower emissions. The measurements were grouped based on emission value in respectively 3 and 4 clusters for the India case (Figure 5.9) and Germany cases (Figure 5.10). The number of clusters were selected to fit and represent variation in the emission. To assess a possible correlation between higher values and the wind direction, the CO emissions were plotted against the wind direction. For the Bhilai Steel Plant, the higher emissions value seem to equally occur for each wind direction (see the right image in Figure 5.9). However, no large variation in wind direction (north-east to east) was found over all Bhilai measurements. The Huttenheim site emission estimates corresponding to a north-west to north-east wind direction coincide with higher emissions. Almost all other measurements with higher values (clusters 2 and 3) occur at the opposite wind direction (south-west to south-east). A large amount of the cluster 2 and 3 values estimated for the adjacent Schwelgern site do correspond with the prominent north-east to north west and south-west wind directions as well.

The plots in Figures 5.11,5.12 and 5.13 represent plumes and their emission profile belonging to different clusters. First of all, the emission profiles for most cases represent more or less a 'plateau' shape (e.g. plots 1 and 2 in Figure 5.11 and plots 1 and 3 in Figure 5.13. The occurrence of two peaks (at around the same peak values) is another recurrent emission profile shape (see plot 3 in Figure 5.12).

The interpretation of the outliers is challenging. Visually, no interpretation for the 'reason' of the lower emission estimated for 13-04-2019 in comparison to the measurements done at 04-10-2019 and 28-02-2019 over Bhilai can be done (Figure 5.11). However, in plot 1, 22-12-2018, the plume from source A/B ends in the plume corresponding to the Bhilai steel plant. The merging of the two plumes seem to affect the emission measured. The ΔCO of the interfered case is around the same value found for the cluster 1 cases presented in plots 2 (04-10-2019) and 4 (28-02-2019). Although two plumes structures, for source A/B and Bhilai Steel Plant (~35 km apart), are found in the Bhilai cases, no complete individual plumes are visible for the detected cases over the Schwelgern and Huttenheim sites (~18 km apart). In plot 4 of Figure 5.13, it can be seen that two plumes merge after beginning separately. Furthermore, two different scenario's can be distinguished: (1) broad merged plumes and (2) the alignment of the two sites with respect to the wind direction (one plume following into the other plume.) For the first scenario, the fixed transects lines of 30 km width do not seem to cover the entire plume width (plots 2 and 4 in Figure 5.13).

The influence of measurements flagged as potentially interfered (flag 2) did not appear to be significant on the overall value obtained from the entire time series (Figure 5.14).

The results were used to test the agreement with stated events. First of all, we test the statement made by Steel Authority of India (SAIL) concerning the continuity of steel operations on the day of a fire incident at 8:30 local time in the coke oven. According to SAIL, there was no disruption of the operations [Drolia, 2019]. Figure 5.15 presents the detected plumes and emission profiles for the 24th of May 2019 (observed CO field at: ~12:42) and 25th of May 2019 over the Bhilai Steel Plant. Activity is detected on the day of the fire and no signs of the occurred fire are seen. The emission estimate for the 24th (clustered as Cluster 0) with 6.61$\pm$0.31 kg/s is slightly lower than the overall time average (8.58$\pm$0.43). The measurement for the 25th containing 9.05$\pm$0.68 kg/s (clustered as Cluster 1) corresponded with the overall average at Bhilai.

Next, an analysis has been done on the first half year 2020 to see the possible effect of the COVID-19 pandemic on the steel plant estimates. The major abrupt decline in global steel production from early 2020 as a

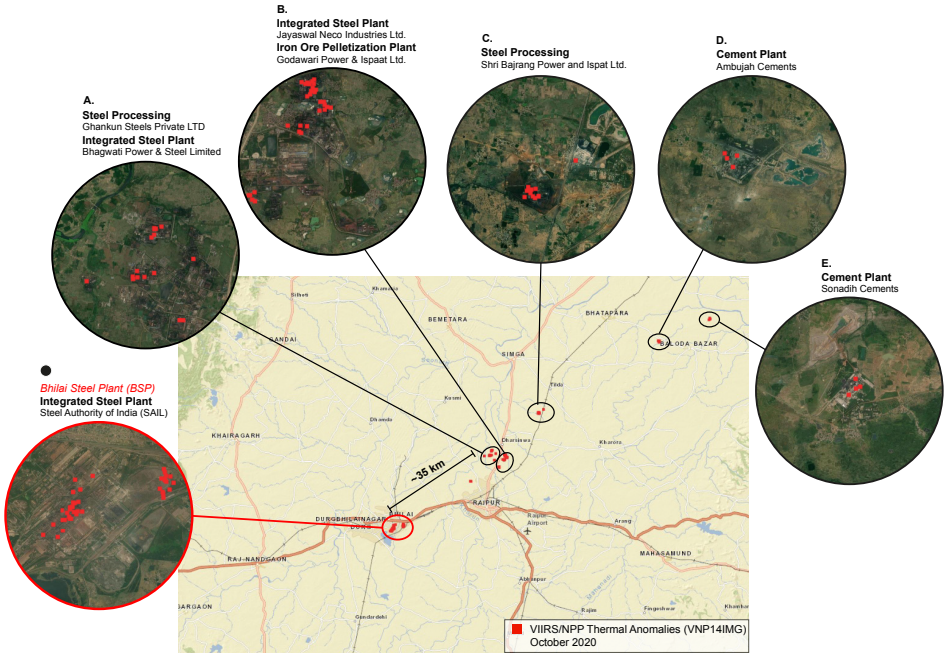

Figure 5.7: Sources located around Bhilai Steel Plant area. Bhilai steel plant (case study by this study) is indicated by red.

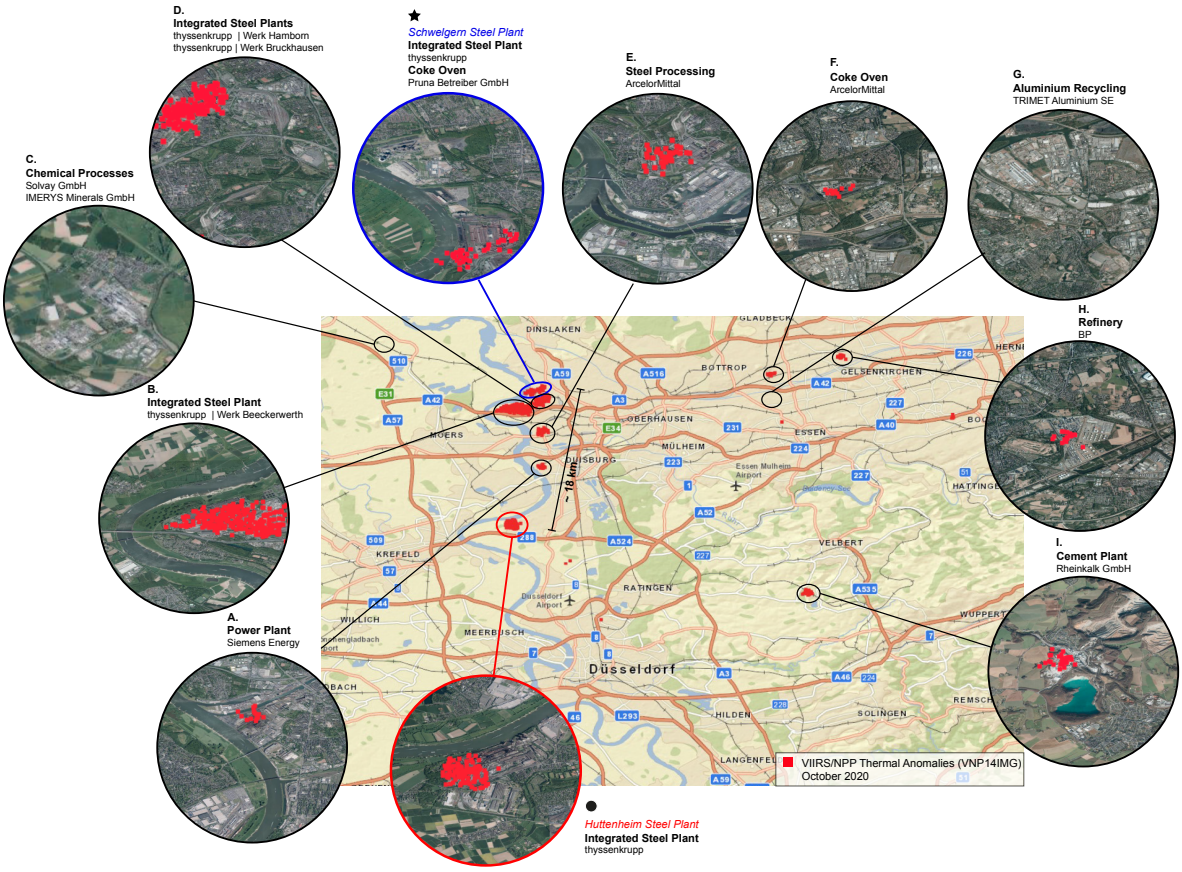

Figure 5.8: Location of ThyssenKrupp sites, both case studies, Huttenheim (indicated by red) and Schwelgern (indicated by blue) (~ 35 km apart). Other sources are indicated by letters (A-I).

Symbol	Type	Company | site	CO Emission (t/yr$_{2017}$)
•	Integrated Steel Plant	thyssenkrupp | Huttenheim	185,000
⋆	Integrated Steel Plant	thyssenkrupp | Schwelgern	117,000
	Coke Oven	Prunk Betreiber GmbH	600
A.	Power Plant	Siemens Energy	-
B.	Integrated Steel Plant	thyssenkrupp | Beeckerwerth	7,300
C.	Chemical Processes	Solvay GmbH	10,700
	Chemical Proccesses	IMERYS Minerals GmbH	1,110
D.	Integrated Steel Plant	thyssenkrupp | Bruckhausen	3,890
	Integrated Steel Plant	thyssenkrupp | Hamborn	4,350
E.	Steel Processing	ArcelorMittal	-
F.	Coke Oven	ArcelorMittal | Bremen	3,130
G.	Aluminium Recycling	Trimet Aluminium SE	13,600
H.	Refinery	BP	-
I.	Cement Plant	Rheinkalk GmbH	3,920

Table 5.1: Sources in the Duisburg area with the symbols corresponding to the locations as indicated in Figure 5.8. The CO Emissions refer to emission as registered in the E-PRTR in tonnes per year.

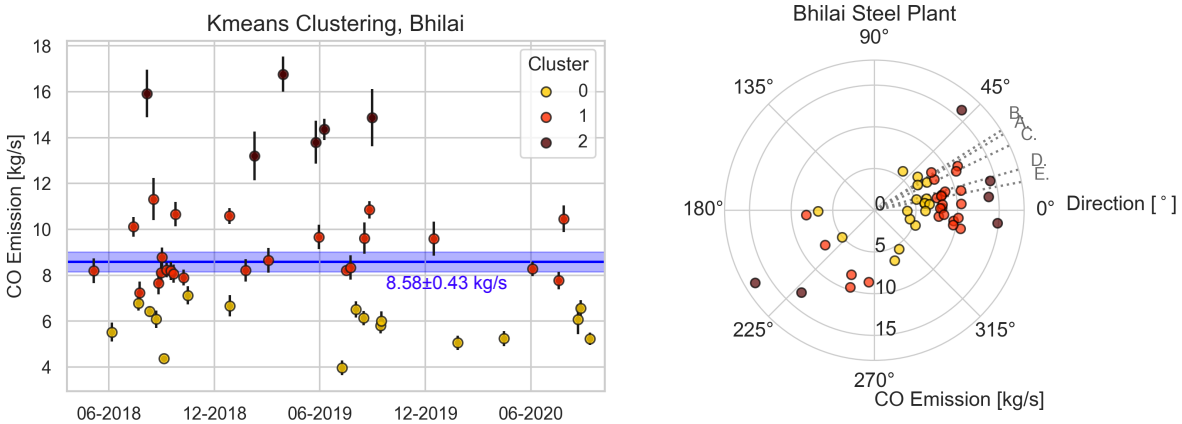

Figure 5.9: Measurements from Bhilai clustered based on emission value using k-means plotted over time (left) and on a polar plot against the wind angle (right). The blue shaded area represents the mean and standard error of the emissions values over the entire time series.

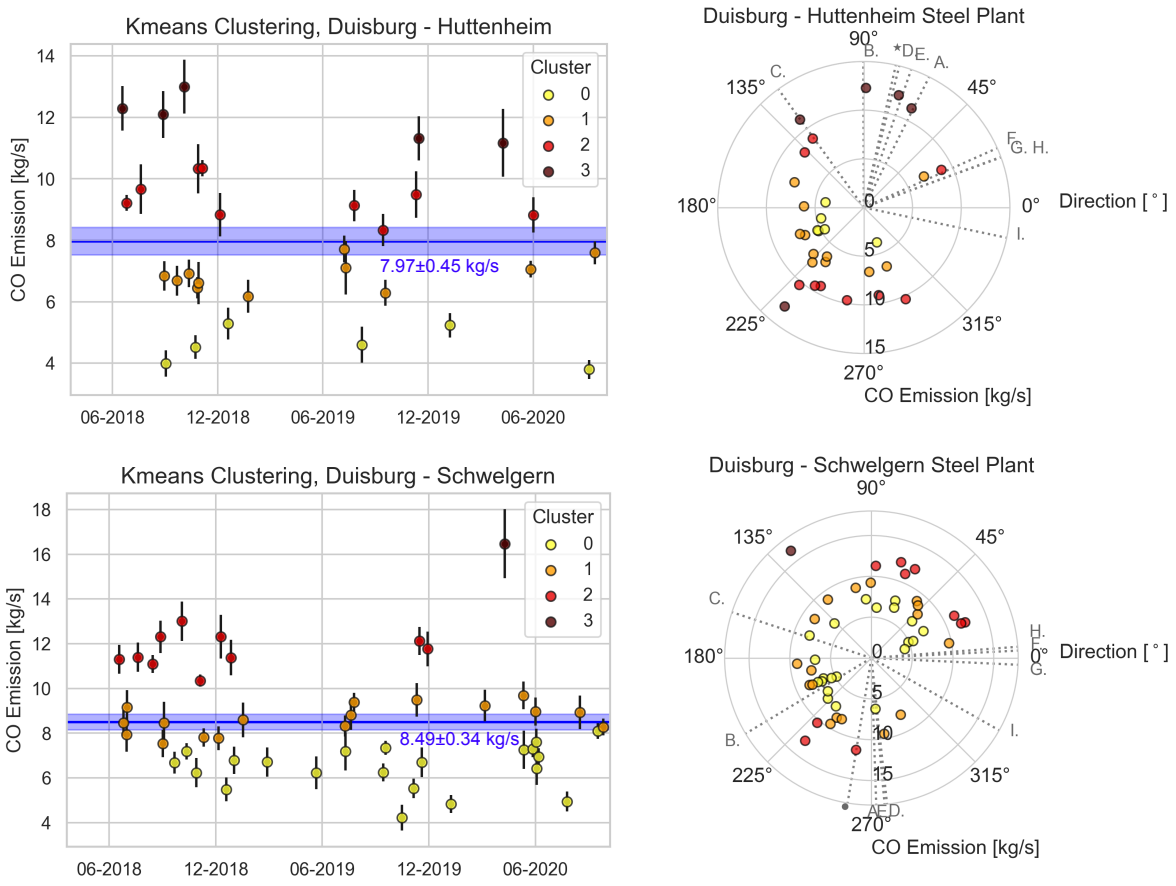

Figure 5.10: Measurements from Duisburg sites Huttenheim (upper) and Schwelgern (bottom) clustered based on emission value using k-means plotted over time (left panel) and on a polar plot against the wind angle (right panel). The blue shaded areas represent the mean and standard error of the emissions values over the entire time series for each site.

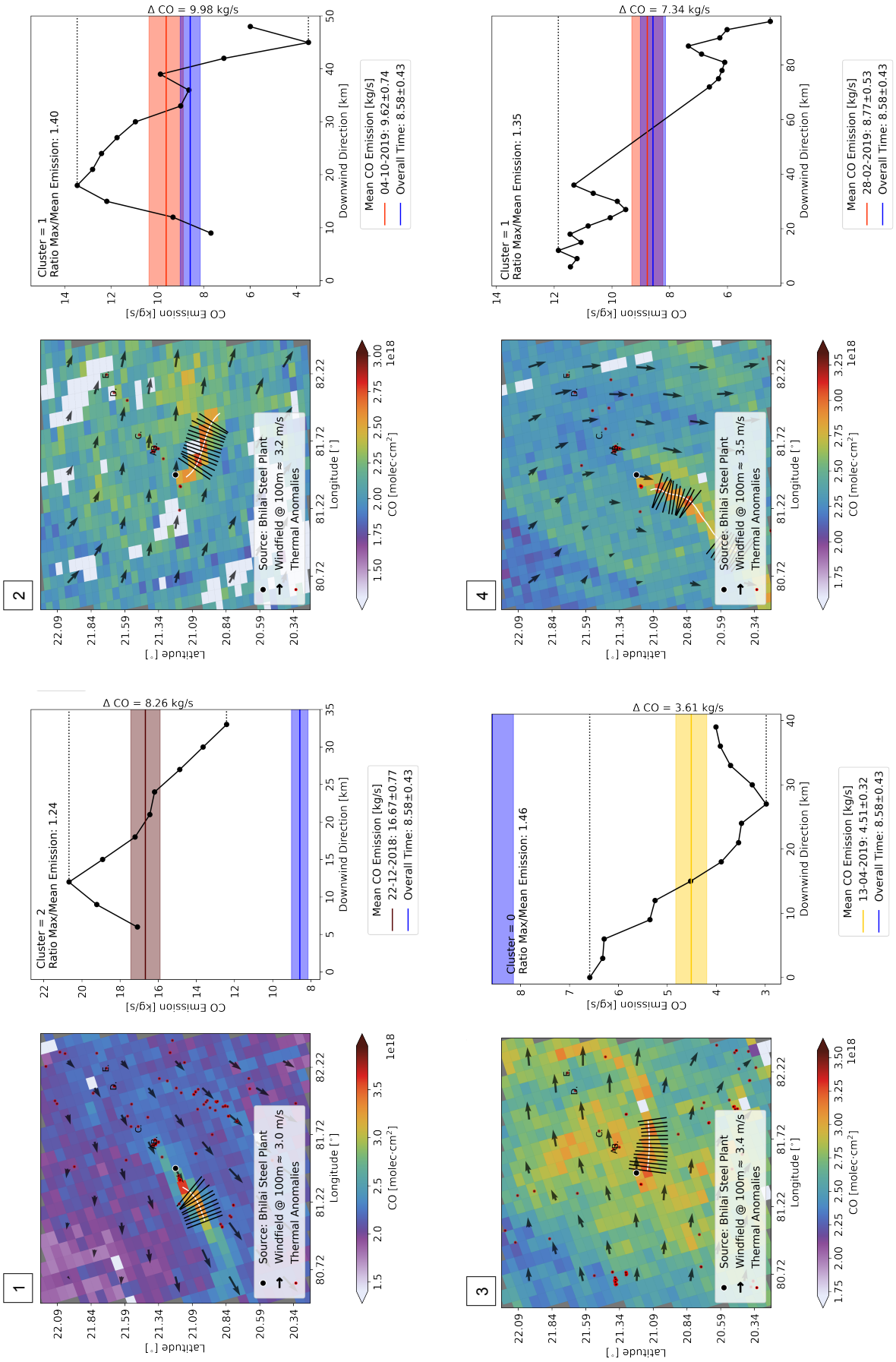

Figure 5.11: Plumes alongside with their emission profile on the right. The blue shaded area corresponds to the mean and error interval from the overall Bhilai Plant. The mean and error of the emission from the specific case is indicated with the color of the corresponding cluster number (as indicated in figure 5.9). Letters indicate the sources as presented in Figure 5.7.

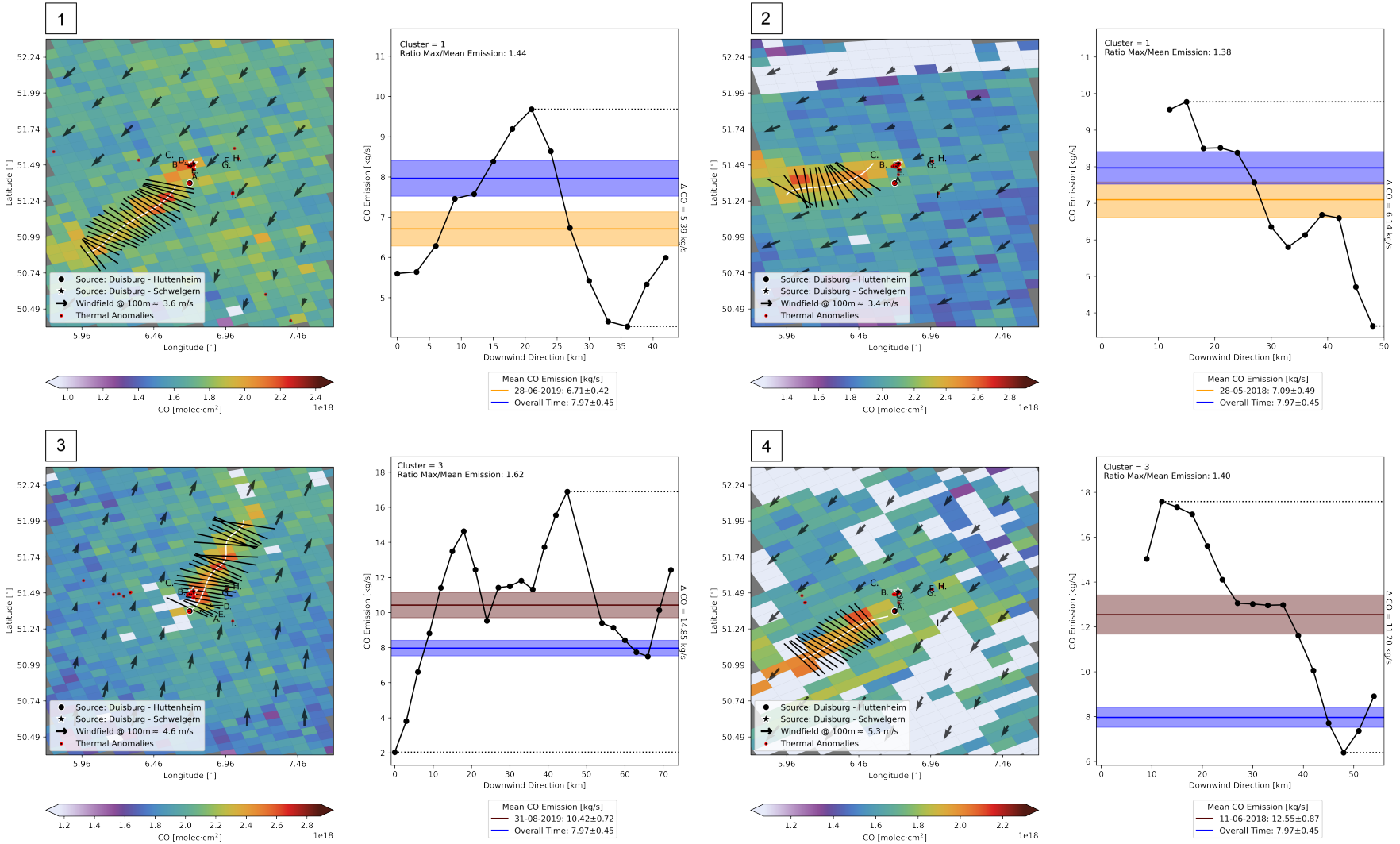

Figure 5.12: Plumes alongside with their emission profile on the right. The blue shaded area corresponds to the mean and error interval from the overall Huttenheim site. The mean and error of the emission from the specific case is indicated with the color of the corresponding cluster number (as indicated in figure 5.10). Letters indicate the sources as presented in Figure 5.8.

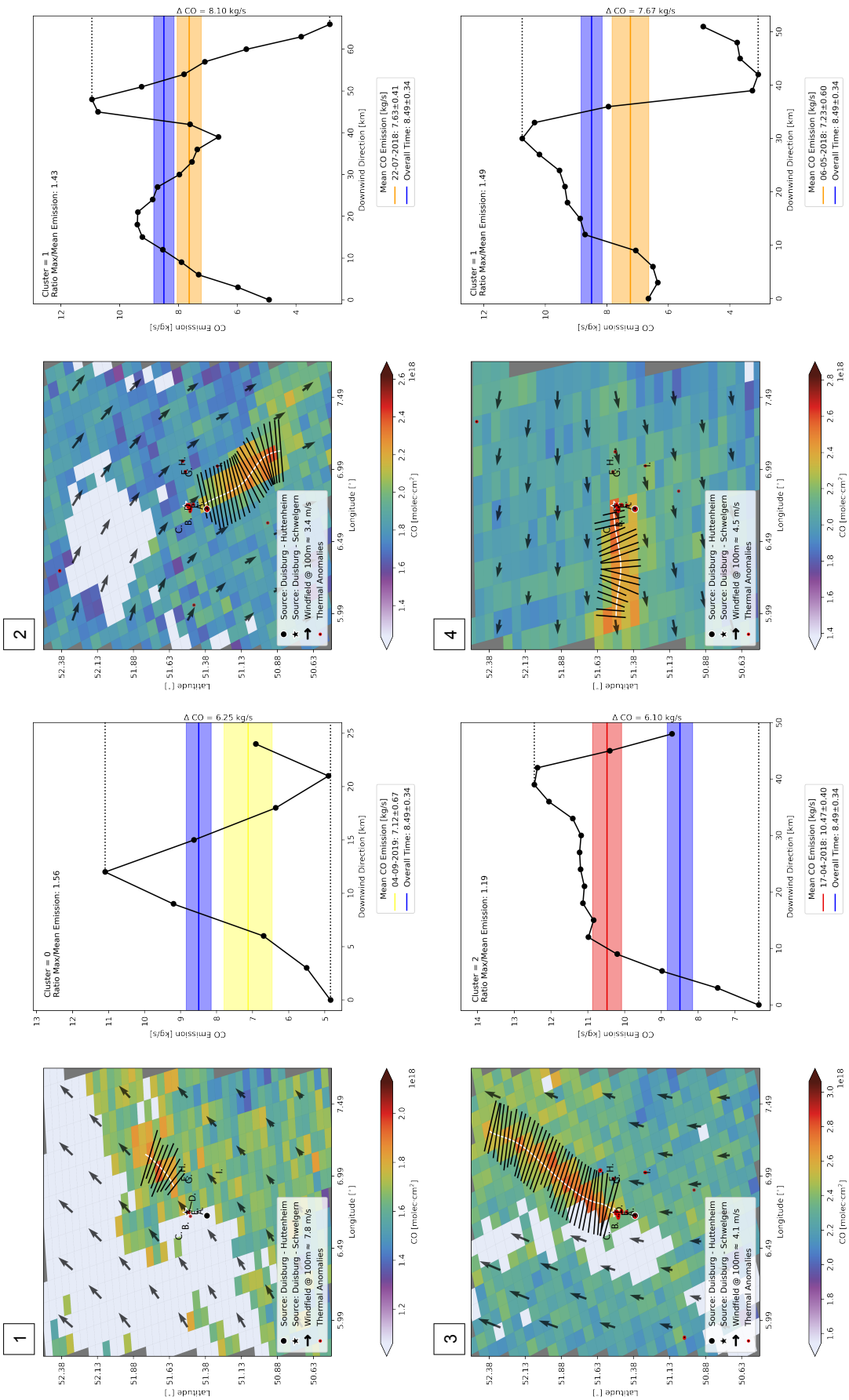

Figure 5.13: Plumes alongside with their emission profile on the right. The blue shaded area corresponds to the mean and error interval from the overall Schwelgern site. The mean and error of the emission from the specific case is indicated with the color of the corresponding cluster number (as indicated in figure 5.10). Letters indicate the sources as presented in Figure 5.8.

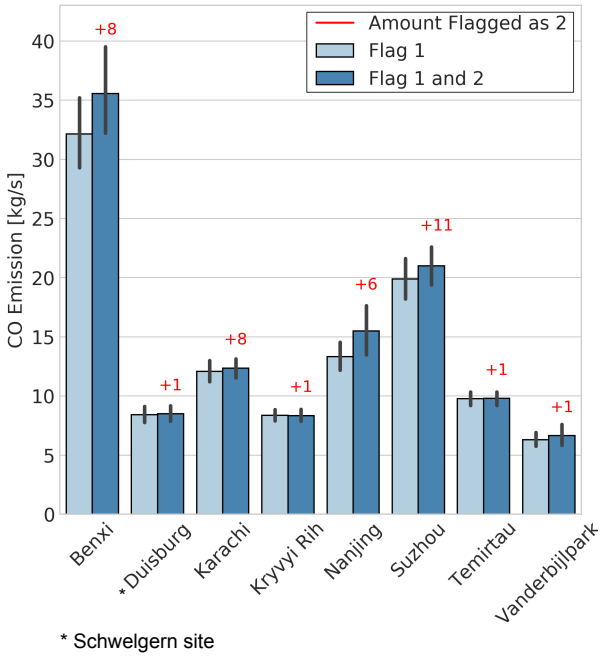

Figure 5.14: CO emissions measured for each facility when accounting only for plumes flagged as 1(true detection and no suspicion of interference by nearby source after visual inspection) or for all true detected plumes. The red numbers indicate the amount of plumes flagged as 2 for each plant. The steel plants listed all have 40 or more measurements and have at least one case flagged as 2. The Duisburg facility concerns the Schwelgern site.

	EU	ACIS	India	China	Developed Asia (DA)
Production with respect to 2019 Q1-Q2	-19.2%	+24.7%	-23.9%	+3.1%	-12.8%

Table 5.2: Difference in steel production of the first half year (Q1-Q2) of 2020 relative to the same period in 2019. Data obtained from [ArcelorMittal, 2020].

result of the COVID-19 pandemic [ArcelorMittal, 2020] (see table 5.2), provided a unique opportunity to test the capability of capturing sudden change in emission patterns using the time series. The regions mentioned by [ArcelorMittal, 2020] concern EU (EU-28), Arcelor Mittal's ACIS segment (e.g. Kryviy Rih in Ukraine, Temirtau in Kazakhstan and Vanderbijlpark in South-Africa), India, China and Developed Asia (Japan, South-Korea and Taiwan). In order to analyze the changes per region, the emission estimates are standardized per facility before converging. We used Median and Median Absolute Deviation based normalization [Kappal et al., 2019] for the standardization:

$$z = \frac{\hat{\mu}_m - x_i}{\hat{\sigma}_m} \tag{5.1}$$

where z is the Z score, $\hat{\mu}_m$ refers to the median of the set x (emission estimates of a specific steel plant) and $\hat{\sigma}_m$ concerns the median absolute deviation. We normalized using the median rather than the mean in order to be more robust to outliers and variation in emission values. Only steel plant with at least 5 measurements over each half year time frame for 2018, 2019 and 2020 were taken into account. A minimum measurements per period was set to better represent each period and to limit bias. A minimum number of 5 was empirically found to both limit the bias by outlier while taking into account the limited number of emission estimates obtained. Figure 5.17 presents the comparison between Q1-Q2 for the periods 2018-2019 and 2020 for the EU, ACIS, India, China and DA regions (corresponding to the regions used in Table 5.2 using different settings for the minimum total amount of emission estimates (covering the first 6 months of 2018-2020) over each plant. Using different combinations of steel plants (due to setting different minimum amount of measurements) to represent the region impacts the overall value (and sign) of the specific region (Figure 5.17). The significant drop as seen in the steel production is not present in Figure 5.17.

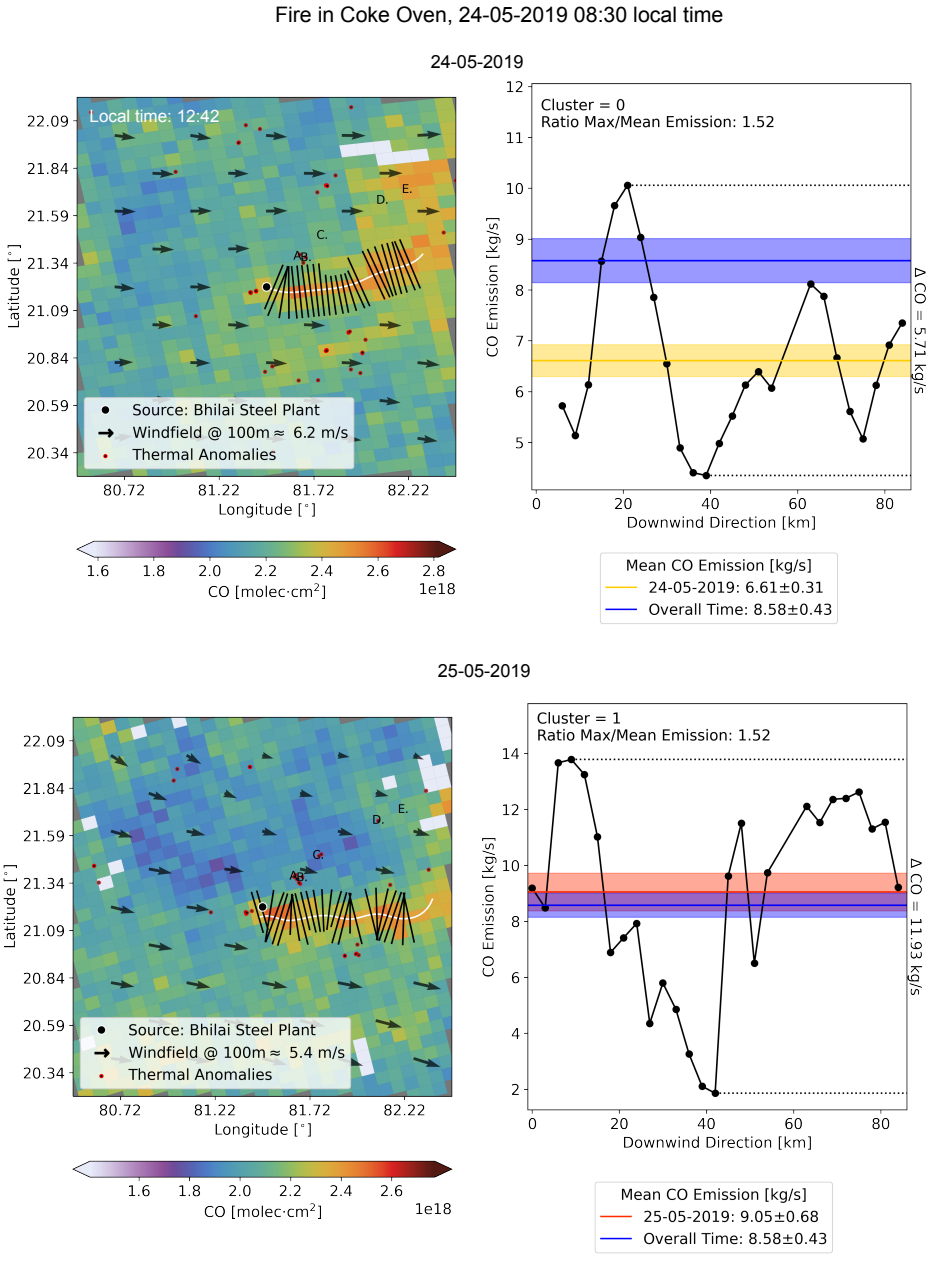

Figure 5.15: Plumes and emission estimates of Bhilai Steel Plant for 24-05-2019 and 24-05-2019. At the 24^{th} of May a fire in the coke oven occurred [Drolia, 2019].

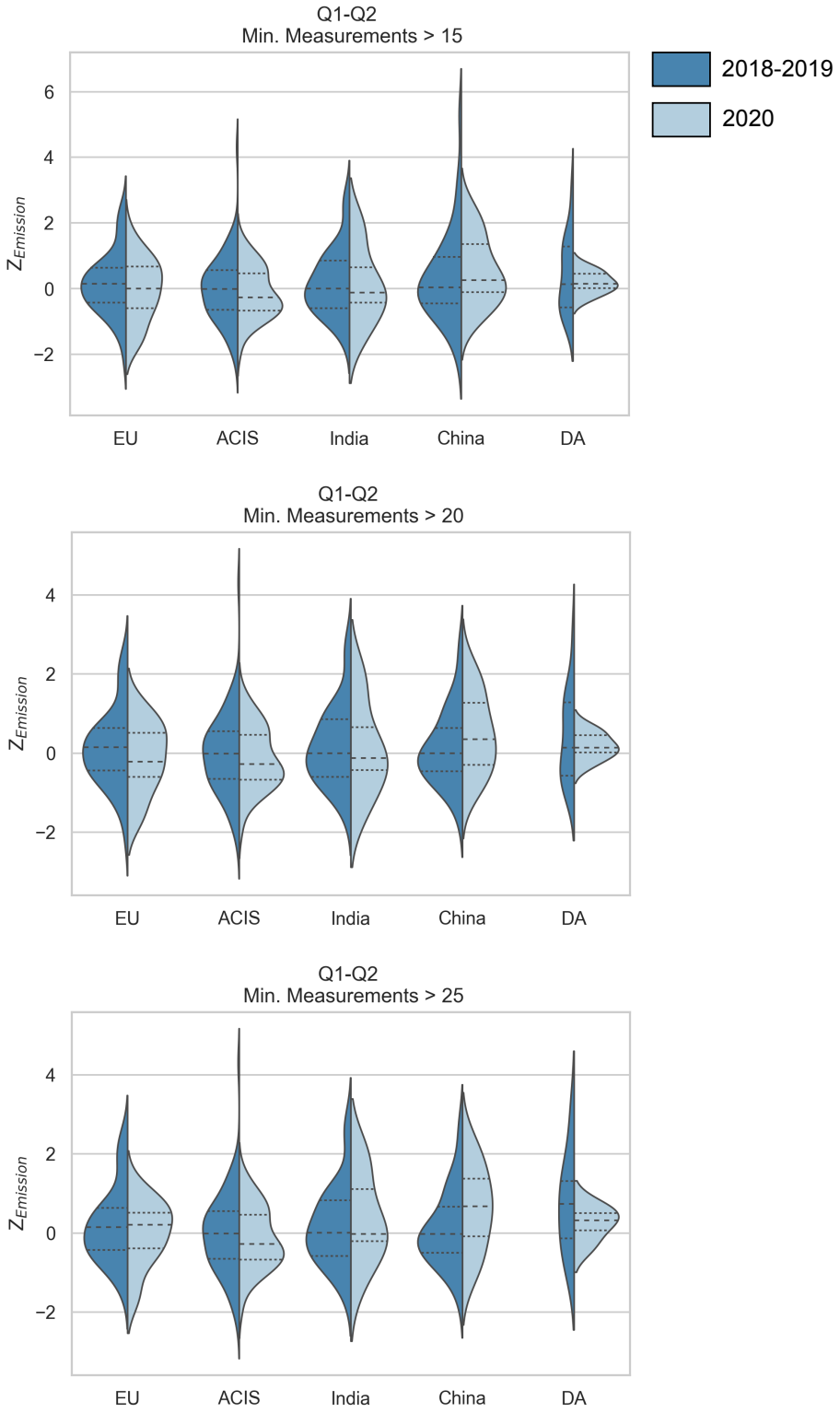

Figure 5.16: Collection of standardized measurements from steel facilities from EU (EU-28), Arcelor Mittal's ACIS segment (e.g. Kryviy Rih in Ukraine, Temirtau in Kazakhstan and Vanderbijlpark in South-Africa), India, China and Developed Asia (Japan, South-Korea and Taiwan) for the first half-year (January - June) of 2018 and 2019 compared to 2020. The dashed lines indicate the quantiles. From top to bottom the images portray the results using a collection of steel plants with more than 15, 20 and 25 measurements. In order to limit influence by potential interference of other sources, we only used measurements flagged as 1.

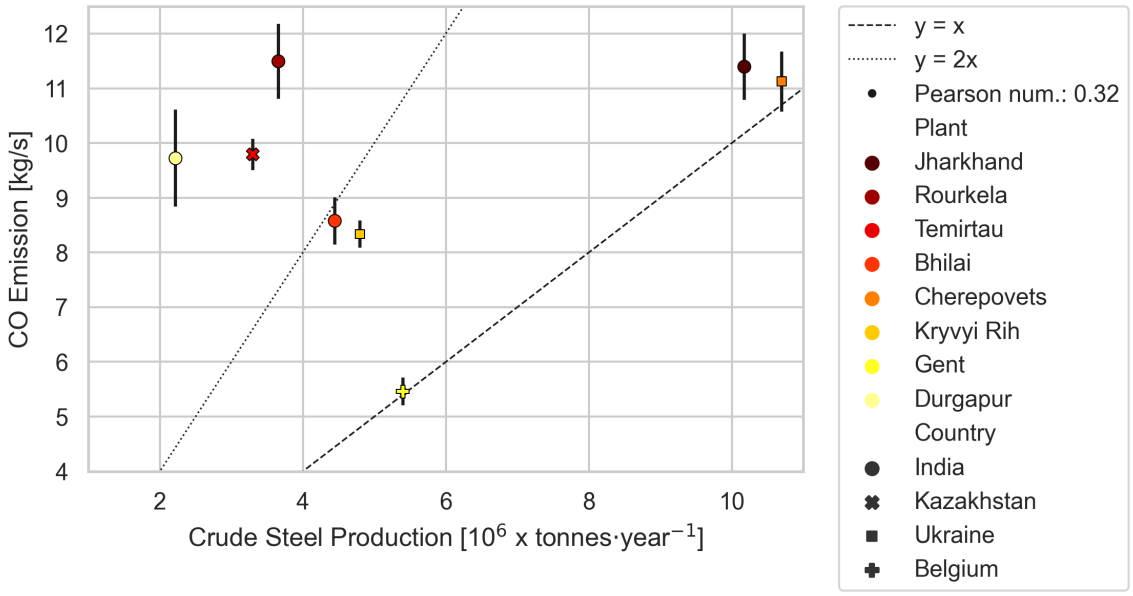

Figure 5.17: The amount of crude steel production plotted against the by this study found CO emissions from several steel plants. The facilities of the portrayed steel plants consist of a Coke oven, Sintering plant and Blast Furnace. Only steel plants with 15 measurements are presented. The error bars indicate the standardized error from the obtained emission estimations per steel plant by this study. he dashed line indicates a linear relation between the crude steel produced in 10^6 tonnes per year and the estimated emission in kg/s, whereas the dashed line portrays an emission of 2 kg/s per 10^6 tonnes crude steel produced per year.

Finally, we analyzed the relation between crude steel production and the obtained emission estimates (Figure 5.17). In order to have a fair comparison, the steel facilities used for the analysis were selected on the (prominent CO emitting) processes. Here we selected steel plants that facilitated the following processes on site: coke oven, sintering and blast furnace. The annual production per steel plant including the source of is presented in Table 6.2. This combination of processes was selected due to high occurrence at integrated steel plants. Furthermore, it should be noted that not all steel plants do report their production numbers publicly. The Pearson Number of 0.32 indicates that there is no clear correlation. The three steel plants (Jharkhand, Cherepovets and Gent) with the largest annual crude steel production (closest to the 'y=x' line) had the lowest emission relative to the production.

6. Discussion and Conclusion

This study was designed to establish the potential of an automated plume detection and emission estimation framework applied on TROPOMI CO data. The framework and its resulting time series were evaluated through the tracking CO emissions from steel plants. Due to limited knowledge of CO emissions from steel plants, great potential could arise. We processed and analyzed the emissions from 132 steel plants worldwide over more than 2.5 years using the developed automatic framework. It was investigated whether the framework could fill the gap of recent registers by enabling comparison among steel plants and insight into fluctuations over time with the needed data quality.

The first step of this work consisted of the development of the operational framework. The final product, as presented in this report, proved to be robust in the meaning that it enabled the detection of plumes over a variety of conditions of e.g. the background variation, plume signal strengths and presence of adjacent plumes. However, the performance of the algorithm was not found constant for all regions. Of the 23.1% through visual inspection discarded measurements, the majority corresponded to steel facilities with a low number of returned measurements. Indicating a lower rate of false detected plumes of facilities with clear and high plume signals. In addition, it was noted that for steel facilities located near coastal area's a large number of measurements had to be manually filtered. A possible explanation could be that the test cases used all did consist of multiple good quality plumes. Thus the empirically found variables to work best as threshold variables may be biased. Finding the right general value for the thresholds to at the same time limit detecting false plumes as well as limiting the rejection of good plumes that applies for all cases appeared to be challenging. From the performance of the algorithm it could be concluded that the framework relies, for a large part, on the execution of the unsupervised filtering step. The filtering steps are applied after the entire processing (detection of plume mask, extraction of the center line and the emission estimation). Thus, a large reliance on the filtering points at a low efficiency of the framework. Optimizing the rejection of undesired cases during the processing steps could lead to a higher efficiency of the framework.

The framework utilizes a mass balance approach to estimate emissions from the detected plume. Following the mass balance approach, the emission rate should equal the discharged mass through the cross-sectional area per unit of time under the assumption of a steady state. Furthermore, the approach can only be applied on wind speed is not smaller than 2 m/s. The double peaks found in the emission profile, could however be the result of a changed wind speed over time causing rapid transportation of the signal farther downwind. The unknown wind height, and thus field, appeared to be the largest uncertainty. This study used the wind field at the height of 100 m above the ground. To validate the use of the assumed effective wind height of 100 meter this study tested the analogy of the wind direction and direction computed from the extracted plume center line. The only small number of measurements that aligned with the 100 meter wind field but not with the 10 meter wind field, indicate the inability of the method to estimate the wind height based on the set requirement. Furthermore, there is a significant difference in the overall steel plant emission that resulted from the 100 m or 10 m wind height assumption. Although the noted uncertainty in the selection of wind speed measurement height, the bias seems systematic allowing the differentiation in overall emissions found at various steel plants.

The second step of this work covered the analysis of the potential of TROPOMI CO observations to map emissions. For a total of 132 tested globally distributed plume facilities, a total of 1,774 plumes were found over 119 facilities. Steel plant facilities are often clustered and/or surrounded by other CO emitters (e.g. cement plants and power plants). This study examined the emission estimates and their variation over time into more depth for a steel facility located in Bhilai, India, and two steel facilities located in Duisburg, Germany,

that are only ~18 km apart. We found that for a distance of 35 km between two plants the individual plumes could be extracted. However this was not the case for the two steel plants that were only 18 km apart.

We were able to find some interesting future applications of our approach. One example is the ability to find back the manufacturer's statement of continuing the operations during a site fire (24th of May 2019 in Bhilai). Our found emission estimate did confirm this statement. We also did an attempt to confirm the significant global drop in steel production during the period of 2020 as the result of COVID-19. It seems that the scattered distribution of measurements and their emission values over time do in fact limit the possibilities to find back this kind of rather detailed difference in a small time frame. One of the main questions we had prior to the start of the analysis was if we could be able to represent the annual data of manufacturers, registered in Pollutant Release Transfer Registers (PRTR). We did analyze the E-PRTR data and compared them for a selection of plants with our estimates. A positive correlation (r = 0.76) between the E-PRTR and our data was found. In fact we did see that for all our plants our estimates were significantly higher than the numbers registered by the facilities in the E-PRTR. This might indicate a structural underestimation by the manufacturers.
We only applied the framework on plumes emerging from steel plants. The framework could be utilized for the emission estimation of other CO emitting point sources with a detectable CO signal, such as bushfires. With the development of the plume detection we aimed to reach a certain robustness to different sizes of plumes. Although the unsupervised filtering (post-processing step) and initial fixated transect width (emission estimation step) were especially designed to fit the characteristics of steel plant plumes, the same or slightly adapted parameters may hold true for other plumes.

We have not been able to interpret all outliers or apparent groups present in the emission estimate values over time for our case studies. We indicated interpretation difficulties through more in depth inspection of the emissions estimated over time for the Bhilai Steel Plant (SAIL), India, and neighboring sites (~18 km apart) Schwelgern and Huttenheim located in Duisburg (ThyssenKrupp), Germany. More understanding regarding factors that could influence a single estimated emission other than the actual production itself will be necessary. Ultimately the gained understanding could help to implement filtering targeted at limiting the interference effect to further optimize the framework.

Our research concerned a first evaluation of utilizing CO observations from TROPOMI to detect and finally estimate the emissions from a large number of steel plants through an automated approach. No extensive analysis was done on identification of properties that allowed or limited the detectability of the carbon monoxide plumes by our framework. Therefore, no complete assessment has been done on, for instance, what regions could benefit most from such an approach. The algorithm was developed through an iterative trial and error approach using multiple steel plant locations that were selected to represent most geographical location.

Unfortunately, the unequal distribution of emission estimates over time limit the analysis over small periods of time. Although, the measurements for multiple plants seemed to be clustered, the identification was difficult. The lack of information regarding production variation over time or the operation of nearby facilities, limited the explanation of higher values. More in depth studies of the emission per steel plant will be necessary. High potential lies in the use of thermal anomalies data for indicating processes.

We show that TROPOMI CO observations enable mapping of pollution from point sources. We conclude that TROPOMI CO observations and the framework proposed in this study illustrate the potential of high resolution space-based instruments to monitor emissions from point sources on an operational level and eventually map global emissions from e.g. industries including those of uncharted sources.

Several recommendations follow from this study:

- The interference of adjacent sources was found to affect the estimated emission. Enabling the detection of interference by the framework itself will limit the amount of outliers. A possible way to implement this in the algorithm is through test the overlapping of other known sources in the area with the specific plume of interest. This could be done in combination with testing of the activity or comparison of the ΔCO of the emission profile in order to assure the potential presence of interference. Detecting the interference is of great importance for the interpretation of detected change in emissions.

- Improving the detection algorithm could improve the resolution over time.

- This study detected 1,774 plumes and demonstrated the potential for the detection of plumes over

various condition. The large number of plumes could be used as training data for the development of a detection algorithm utilizing a machine learning approach.

- The FIRMS fire counts used to manually identify steel plants could be used to automatically detect sources.

Appendix

Table 6.1: Information regarding the listed steel plants by this study: the latitude, longitude, country. Furthermore the results from the framework, number of estimates and mean emission value estimated plus minus the standard error, are presented as well.

Steel Plant	Latitude	Longitude	Country	Num. Estimates	Emission Estimate [kg/s]
Bethioua	35.773114	-0.258498	Algeria	0	
PortKembla	-34.4668	150.8886	Australia	1	7.02±0.00
Linz	48.279226	14.3268	Austria	5	13.10±1.57
Donawitz	47.0338	15.0678	Austria	0	
Chakda	23.670907	90.454820	Bangladesh	6	5.61±0.41
Shahariar	23.717	90.446	Bangladesh	15	5.30±0.36
Gent	51.1767	3.8144	Belgium	23	5.46±0.26
VoltaRedonda	-22.5116	-44.1143	Brasil	0	
OuroBranco	-20.5467	-43.7640	Brasil	0	
Jeceaba	-20.585365	-43.961878	Brasil	0	
RioDeJaneiro	-22.9167	-43.7477	Brasil	0	
SaultSteMarie	46.5247	-84.3681	Canada	0	
Hamilton	43.2694	-79.8247	Canada	0	
Beijing	39.9017	116.158	China	0	
Benxi	41.2329	123.6370	China	42	35.55±1.93
Tangshan	39.7304	118.4667	China	29	47.60±3.41
Huangshi	30.204	115.150	China	1	14.09±0.00
Xiangtan	27.8118	112.8974	China	23	10.58±0.64
Huaian	33.557629	118.993680	China	13	7.90±0.65
Suzhou	31.977203	120.630473	China	62	21.00±0.83
Shizuishan	39.43	106.7	China	11	27.14±4.90
Wuhan	28.2242	112.9881	China	4	9.48±1.50
Chongqing	29.807402	107.066503	China	3	9.83±2.39
Taiyuan	37.9192	112.5387	China	5	18.33±3.70
Nanjing	32.1892	118.7453	China	42	15.48±1.08
Maanshan	31.7425	118.4754	China	32	16.23±1.20

Rizhao	35.1610	119.3578	China	21	38.45±3.23
Lubumbashi	-11.580589	27.487375	Congo	8	13.03±4.57
Ostrava	49.7959	18.3058	CzechRepublic	12	7.29±0.56
Trinec	49.6881	18.64728	CzechRepublic	4	6.80±0.85
Suez	29.641905	32.278939	Egypt	0	
Dunkerque	51.03	2.36	France	12	5.54±0.22
FosSurMer	43.45	4.9	France	1	3.28±0.00
Seremange-Erzange	49.3238	6.0948	France	3	5.99±1.24
GrandeSynthe	51.034523	2.283082	France	11	6.33±0.51
Eisenhuttenstadt	52.1661	14.61768	Germany	1	2.57±0.00
Dillinger	49.3572	6.7541	Germany	30	5.76±0.20
Hennigsdorf	52.649108	13.211126	Germany	1	6.47±0.00
Salzgitter	52.1548	10.4031	Germany	19	4.70±0.25
Volklingen	49.2459	6.8462	Germany	22	5.61±0.25
Bremen	53.1249	8.6867	Germany	9	4.65±0.29
Dessau	51.50369	6.7359	Germany	49	8.49±0.34
Duisburg	51.36823	6.71227	Germany	31	7.97±0.45
Dunaujvaros	46.9395	18.9389	Hungary	3	5.68±1.14
Fjaroabyggo	65.0338	-14.0997	Iceland	0	
Rourkela	22.2209	84.7605	India	20	11.49±0.68
Jharkhand	22.7897	86.1985	India	26	11.39±0.60
Asansol	23.6624	86.1985	India	36	13.60±0.94
Bhadravati	13.8369	75.7020	India	0	
Durgapur	23.4986	87.3712	India	24	9.72±0.89
Dolvi	18.6926	73.0366	India	0	
Tadipatri	14.8778	78.044	India	0	
Visakhapatnam	17.617	83.193	India	11	17.30±2.15
Bamunari	22.7175	88.306	India	5	7.79±0.80
KurruBhantha	21.981	83.241	India	9	7.74±0.92
Gujarat	23.1062	70.1868	India	7	4.19±0.44
Kalinganagar	20.9704	86.0082	India	6	6.21±1.23
Bhilai	21.2189	81.4727	India	47	8.58±0.43
Bokaro	23.7857	85.883712	India	13	11.76±0.72
Salem	11.6617	78.0279	India	1	7.76±0.00
Fatufia	-2.831	122.168	Indonesia	0	
Samangraya	-6.003915	105.9947	Indonesia	0	
BandarAbbas	27.1562	56.0845	Iran	0	

Chadormalu	32.3865	53.7476	Iran	1	3.17±0.00
Muroran	42.340686	141.007035	Japan	0	
Kashima	35.928737	140.679364	Japan	5	7.09±0.75
Kurashiki	34.513664	133.716439	Japan	17	17.19±1.22
Nakabaru	33.9200	130.844593	Japan	2	8.14±1.01
Chiba	35.583358	140.099003	Japan	6	10.53±1.23
Oita	33.259	131.6416	Japan	2	10.17±2.07
Tokai	35.031682	136.876335	Japan	11	13.22±1.71
Fukuyama	34.470887	133.436415	Japan	13	15.58±1.26
Temirtau	50.04464	73.0321	Kazakhstan	119	9.79±0.29
Misratah	32.333846	15.2113418	Libya	3	9.94±2.50
Guerrero	25.7212	-100.2995	Mexico	0	
Lazaro	17.929961	-102.20523	Mexico	8	13.46±0.95
IJmuiden	52.47656	4.59217	Netherlands	1	5.41±0.00
AlNoor	31.607	74.368	Pakistan	22	8.63±0.49
Karachi	24.802	67.343	Pakistan	51	12.34±0.41
Zdzieszowice	50.4230	18.1435	Poland	6	7.25±0.84
Krakow	50.083115	20.0745	Poland	3	9.05±1.06
Dabrowie	50.3434	19.2819	Poland	19	8.09±0.86
Galati	45.43767	27.9779	Romania	14	3.74±0.35
Dorozhnaya	53.218928	45.223802	Russia	1	2.79±0.00
Tsjeljabinsk	55.259	61.443	Russia	40	8.09±0.35
Magnitogorsk	53.5788	51.9421	Russia	3	6.71±0.11
Tula	54.155	37.727	Russia	12	5.60±0.61
Cherepovets	59.141300	37.889598	Russia	42	11.12±0.55
Wolgograd	48.4875	44.6615	Russia	4	3.81±0.33
Novotroitsk	51.2158	58.3669	Russia	26	5.10±0.43
NizhnyTagil	57.9196	60.0316	Russia	4	6.29±1.43
Lipetsk	52.603281	39.620838	Russia	77	9.79±0.35
Borovsky	55.231980	36.679840	Russia	1	4.76±0.00
Kaloega	55.2321	36.6764	Russia	2	3.93±0.59
Nizhnekamskay	55.5788	51.9421	Russia	6	4.05±0.35
Dammam	26.2435	49.9645	Saudi-Arabia	9	12.44±1.56
Sremska	44.977	19.648	Serbia	0	
Kosice	48.6178	21.1983	Slovakia	6	10.32±1.83
VanderBijlPark	-26.661	27.809	South Africa	54	6.64±0.47
Newcastle	-27.700	30.001	South Africa	16	10.54±3.75

Pohang	36.0077	129.3930	South Korea	5	13.66±2.71
GeumhoDong	34.933638	127.735654	South Korea	24	22.39±1.67
Dangjin	36.990199	126.695899	South Korea	45	11.13±0.54
Gijon	43.55611	-5.9111	Spain	1	5.35±0.00
Taranto	40.5167	17.2	Spain	0	
Kaohsiung	22.553400	120.356293	Taiwan	1	41.76±0.00
DarEsSalaam	-6.761	39.240	Tanzania	0	
BangPakong	13.495210	100.972	Thailand	0	
Hatay	36.742129	36.203880	Turkey	0	
Scunthorpe	53.586377	-0.6143	UK	10	5.40±0.37
PortTalbot	51.5679	-3.7595	UK	0	
Gary	41.6125	-87.3144	US	6	9.53±1.85
Ashland	38.4978	-82.6689	US	0	
Bourbonnais	41.182737	-87.855009	US	0	
Butler	40.8482	-79.9204	US	0	
Cartersville	34.244684	-84.797188	US	0	
Charlotte	35.340624	-80.827009	US	0	
Coshocton	40.2076	-81.8821	US	3	2.39±0.30
BurnsHarbor	41.634	-87.131	US	6	9.84±1.13
EastIndianaHarbor	41.6619	-87.4418	US	6	10.12±1.61
Memphis	35.050258	-90.163344	US	0	
Midlothian	32.462176	-97.028404	US	1	10.42±0.00
Marietta	39.37028	-81.5236	US	0	
Ferndale	48.8455	-122.7055	US	0	
WestIndianaHarbor	41.651165	-87.45917	US	6	11.08±1.48
Cleveland	41.472421	-81.66779	US	0	
Crawfordsville	39.975871	-86.822788	US	0	
Zaporizhstal	47.8621	35.1663	Ukraine	74	7.89±0.27
Donetsk	47.103812	37.585712	Ukraine	41	14.48±0.98
Dniprovazhmash	48.475020	34.960459	Ukraine	21	8.16±0.91
Kryvy	47.873923	33.416452	Ukraine	114	8.34±0.25
Mariupol	47.0953	37.5944	Ukraine	45	14.75±0.97

Table 6.2: Crude steel production per steel facility. The steel plants all facilitate a coke oven, sintering plant and blast oxygen furnace.

Steel Plant	Country	Company	Crude Steel Production [10^3 × tonnes/year]	Year	Source
Jharkhand	India	Tata Steel	10,175	2019	[Ministry of Steel , 2019]
Rourkela	India	SAIL	3,658	2019	[Ministry of Steel , 2019]
Bhilai	India	SAIL	4,447	2019	[SAIL, 2020a]
Durgapur	India	SAIL	2,219	2019	[SAIL, 2020b]
Temirtau	Kazakhstan	ArcelorMittal	3,300	2018	[ArcelorMittal, 2019]
Cherepovets	Russia	Severstal	10,700	2013	[Severstal, 2020]
Gent	Belgium	ArcelorMittal	5,400	2018	[ArcelorMittal, 2020b]
Kryvyi Rih	Ukraine	ArcelorMittal	4800	2018	[ArcelorMittal, 2020a]

Bibliography

ArcelorMittal (2019). Fact book 2019. Accessed at 21-09-2020. Obtained from https://corporate-media.arcelormittal.com/media/4sjfifdj/factbook-2019.pdf.

ArcelorMittal (2020). *Interim Financial Report. Half Year ended June 30,2020*. Accessed at 20-08-2020. https://corporate-media.arcelormittal.com/media/hv5j2osz/2020-half-year-report.pdf.

ArcelorMittal (2020a). Metallurgical production. Accessed at 21-09-2020. Obtained from https://ukraine.arcelormittal.com/index.php?id=240.

ArcelorMittal (2020b). Our mills - arcelormittal gent. Accessed at 21-09-2020. Obtained from https://flateurope.arcelormittal.com/ourmills/be/gent.

Aschbacher, J. and Milagro-Pérez, M. P. (2012). The european earth monitoring (gmes) programme: Status and perspectives. *Remote Sensing of Environment*, 120:3–8.

Bankhead, P., Scholfield, C. N., McGeown, J. G., and Curtis, T. M. (2012). Fast retinal vessel detection and measurement using wavelets and edge location refinement. *PloS one*, 7(3).

Beirle, S., Borger, C., Dörner, S., Li, A., Hu, Z., Liu, F., Wang, Y., and Wagner, T. (2019). Pinpointing nitrogen oxide emissions from space. *Science advances*, 5(11):eaax9800.

Borsdorff, T., García Reynoso, A., Maldonado, G., Mar-Morales, B., Stremme, W., Grutter, M., and Landgraf, J. (2020). Monitoring co emissions of the metropolis mexico city using tropomi co observations. *Atmospheric Chemistry and Physics Discussions*, pages 1–21.

Borsdorff, T., Hu, H., Hasekamp, O., Sussmann, R., Rettinger, M., Hase, F., Gross, J., Schneider, M., Garcia, O., Stremme, W., et al. (2018). Mapping carbon monoxide pollution from space down to city scales with daily global coverage. *Atmospheric Measurement Techniques*, 11(10):5507–5518.

Borsdorff, T., Pandey, S., Hasekamp, O., Aben, I., Houweling, S., Landgraf, J., et al. (2019). Carbon monoxide air pollution on sub-city scales and along arterial roads detected by the tropospheric monitoring instrument. *Atmospheric Chemistry & Physics*, 19(6).

Bovensmann, H., Burrows, J., Buchwitz, M., Frerick, J., Noël, S., Rozanov, V., Chance, K., and Goede, A. (1999). Sciamachy: Mission objectives and measurement modes. *Journal of the atmospheric sciences*, 56(2):127–150.

Broquet, G., Bréon, F.-M., Renault, E., Buchwitz, M., Reuter, M., Bovensmann, H., Chevallier, F., Wu, L., and Ciais, P. (2018). The potential of satellite spectro-imagery for monitoring co 2 emissions from large cities. *Atmospheric Measurement Techniques*, 11(2):681.

Brunner, D., Kuhlmann, G., Marshall, J., Clément, V., Fuhrer, O., Broquet, G., Loscher, A., and Meijer, Y. (2019). Accounting for the vertical distribution of emissions in atmospheric co2 simulations. *Atmospheric Chemistry and Physics*, 19(7):4541–4559.

Cambaliza, M., Shepson, P., Bogner, J., Caulton, D., Stirm, B., Sweeney, C., Montzka, S., Gurney, K., Spokas, K., Salmon, O., et al. (2015). Quantification and source apportionment of the methane emission flux from the city of indianapolis. *Elem Sci Anth*, 3.

Cambaliza, M., Shepson, P., Caulton, D., Stirm, B., Samarov, D., Gurney, K., Turnbull, J., Davis, K. J., Possolo, A., Karion, A., et al. (2014). Assessment of uncertainties of an aircraft-based mass balance approach for quantifying urban greenhouse gas emissions. *Atmos. Chem. Phys*, 14(17):9029–9050.

Connors, V. S., Gormsen, B. B., Nolf, S., and Reichle Jr, H. G. (1999). Spaceborne observations of the global distribution of carbon monoxide in the middle troposphere during april and october 1994. *Journal of Geophysical Research: Atmospheres*, 104(D17):21455–21470.

Copernicus Climate Change Service (C3S) (2017). Era5: Fifth generation of ecmwf atmospheric reanalyses of the global climate. Accessed at 08-10-2020. Obtained from `https://cds.climate.copernicus.eu/cdsapp#!/home`.

De Laat, A., Lelieveld, J., Roelofs, G., Dickerson, R., and Lobert, J. (2001). Source analysis of carbon monoxide pollution during indoex 1999. *Journal of Geophysical Research: Atmospheres*, 106(D22):28481–28495.

Dekker, I., Houweling, S., Aben, I., Röckmann, T., Krol, M., Deeter, M., and Worden, H. (2017). Quantification of co emissions from the city of madrid using mopitt satellite retrievals and wrf simulations. *Atmospheric chemistry and physics*, 17:14675–14694.

Denmead, O., Harper, L., Freney, J., Griffith, D., Leuning, R., and Sharpe, R. (1998). A mass balance method for non-intrusive measurements of surface-air trace gas exchange. *Atmospheric Environment*, 32(21):3679–3688.

Dios, M., Morán, M., Carrera, F., Pombo, C., Souto, J. A., Casares, J. J., Díaz, A., and Saez, A. (2013). Prtrval: A software tool for the validation of european pollutant release and transfer register emissions data. In *Proceedings of the 15th International Conference on Harmonization within Atmospheric Dispersion Modeling for Regulatory Purposes*.

Dong, Y. X. (2014). Review of otsu segmentation algorithm. In *Advanced Materials Research*.

Drolia, R. (2019). Chhattisgarh: Fire at sail's bhilai steel plant; no casualty. *The Times of India*. Accessed at 20-01-2021. https://timesofindia.indiatimes.com/city/raipur/fire-at-sails-bhilai-steel-plant-no-loss-of-lives/articleshow/69478183.cms.

ECMWF (2020). Era5: data documentation. Accessed at 08-10-2020. `https://confluence.ecmwf.int/display/CKB/ERA5$%$3A+data+documentation`.

ESRI, D., GeoEye, E. G., et al. (2018). World imagery.

European Commission (2006). Guidance document for the implementation of the european prtr. Obtained from `https://prtr.eea.europa.eu/#/downloadguidance`.

Ge, C., Wang, J., Carn, S., Yang, K., Ginoux, P., and Krotkov, N. (2016). Satellite-based global volcanic so2 emissions and sulfate direct radiative forcing during 2005–2012. *Journal of Geophysical Research: Atmospheres*, 121(7):3446–3464.

Goh, T. Y., Basah, S. N., Yazid, H., Safar, M. J. A., and Saad, F. S. A. (2018). Performance analysis of image thresholding: Otsu technique. *Measurement*, 114:298–307.

González-Jorge, H., González-deSantos, L. M., Martínez-Sánchez, J., Sánchez-Rodríguez, A., and Lorenzo, H. (2018). Automatic measurement of water height in the as conchas (spain) reservoir using sentinel 2 and aerial lidar data. *Remote Sensing*, 10(6):902.

Gordon, M., Li, S., Staebler, R., Darlington, A., Hayden, K., O'Brien, J., and Wolde, M. (2015). Determining air pollutant emission rates based on mass balance using airborne measurement data over the alberta oil sands operations. *Atmospheric Measurement Techniques*, 8(9):3745.

Holloway, T., Levy, H., and Kasibhatla, P. (2000). Global distribution of carbon monoxide. *Journal of Geophysical Research: Atmospheres*, 105(D10):12123–12147.

Janssens-Maenhout, G., Pinty, B., Dowell, M., Zunker, H., Andersson, E., Balsamo, G., Bézy, J.-L., Brunhes, T., Bösch, H., Bojkov, B., et al. (2020). Toward an operational anthropogenic co2 emissions monitoring and verification support capacity. *Bulletin of the American Meteorological Society*, 101(8):E1439–E1451.

Kappal, S. et al. (2019). Data normalization using median median absolute deviation mmad based z-score for robust predictions vs. min–max normalization. *London Journal of Research in Science: Natural and Formal*.

Khalil, M. and Rasmussen, R. (1984). Carbon monoxide in the earth's atmosphere: increasing trend. *Science*, 224(4644):54–56.

KNMI (2019). Sentinel 5 precursor/tropomi knmi and sron level 2 input output data definition. `http://www.tropomi.eu/sites/default/files/files/SRON_S5P_LEV2_RP_002_issue1.10_CO_signed.pdf`.

Kolominskas, C. and Sullivan, R. (2004). Improving cleaner production through pollutant release and transfer register reporting processes. *Journal of Cleaner Production*, 12(7):713–724.

Kong, H., Akakin, H. C., and Sarma, S. E. (2013). A generalized laplacian of gaussian filter for blob detection and its applications. *IEEE transactions on cybernetics*, 43(6):1719–1733.

Kourtidis, K., Georgoulias, A. K., Mijling, B., Zhang, Q., Ding, J., et al. (2018). A new method for deriving trace gas emission inventories from satellite observations: The case of so2 over china. *Science of The Total Environment*, 612:923–930.

Krings, T., Gerilowski, K., Buchwitz, M., Hartmann, J., Sachs, T., Erzinger, J., Burrows, J., and Bovensmann, H. (2013). Quantification of methane emission rates from coal mine ventilation shafts using airborne remote sensing data. *Atmospheric Measurement Techniques*, 6(1):151–166.

Krotkov, N. A., McLinden, C. A., Li, C., Lamsal, L. N., Celarier, E. A., Marchenko, S. V., Swartz, W. H., Bucsela, E. J., Joiner, J., Duncan, B. N., et al. (2016). Aura omi observations of regional so 2 and no 2 pollution changes from 2005 to 2015. *Atmospheric Chemistry and Physics*, 16(7):4605.

Kruszynski, K. J., van Liere, R., Kaandorp, J. A., et al. (2006). An interactive visualization system for quantifying coral structures. In *EuroVis*, pages 283–290.

Kuhlmann, G., Broquet, G., Marshall, J., Clément, V., Löscher, A., Meijer, Y., and Brunner, D. (2019). Detectability of co 2 emission plumes of cities and power plants with the copernicus anthropogenic co 2 monitoring (co 2 m) mission. *Atmospheric Measurement Techniques*, 12(12):6695–6719.

Kuhlmann, G., Brunner, D., Broquet, G., and Meijer, Y. (2020). Quantifying co 2 emissions of a city with the copernicus anthropogenic co 2 monitoring satellite mission. *Atmospheric Measurement Techniques Discussions*, pages 1–33.

Kumar, D., Pramanik, A., Kar, S. S., and Maity, S. P. (2016). Retinal blood vessel segmentation using matched filter and laplacian of gaussian. In *2016 International Conference on Signal Processing and Communications (SPCOM)*, pages 1–5. IEEE.

Kumar, S., Torres, C., Ulutan, O., Ayasse, A., Roberts, D., and Manjunath, B. (2020). Deep remote sensing methods for methane detection in overhead hyperspectral imagery. In *The IEEE Winter Conference on Applications of Computer Vision*, pages 1776–1785.

Laganiere, R. (1998). A morphological operator for corner detection. *Pattern Recognition*, 31(11):1643–1652.

Landgraf, J., aan de Brugh, J., Scheepmaker, R., Borsdorff, T., Houweling, S., and Hasekamp, O. (2018). Algorithm theoretical baseline document for sentinel-5 precursor: Carbon monoxide total column retrieval. `http://www.tropomi.eu/sites/default/files/files/SRON_S5P_LEV2_RP_002_issue1.10_CO_signed.pdf`.

Landgraf, J., Borsdorff, T., Langerock, B., and Keppens, A. (2019). S5p mission performance centre nitrogen dioxide [*L2__CO___*] readme. `http://www.tropomi.eu/sites/default/files/files/publicSentinel-5P-Carbon-Monoxide-Level-2-Product-Readme-File.pdf`.

Landgraf, J., Scheepmaker, R., Borsdorff, T., Hu, H., Houweling, S., Butz, A., Aben, I., Hasekamp, O., et al. (2016). Carbon monoxide total column retrievals from tropomi shortwave infrared measurements. *Atmospheric Measurement Techniques (AMT)*, 9:4955–4975.

Lavoie, T. N., Shepson, P. B., Cambaliza, M. O., Stirm, B. H., Karion, A., Sweeney, C., Yacovitch, T. I., Herndon, S. C., Lan, X., and Lyon, D. (2015). Aircraft-based measurements of point source methane emissions in the barnett shale basin. *Environmental Science & Technology*, 49(13):7904–7913.

Levy, R. J. (2015). Carbon monoxide pollution and neurodevelopment: a public health concern. *Neurotoxicology and teratology*, 49:31–40.

Li, C., Zhang, Q., Krotkov, N. A., Streets, D. G., He, K., Tsay, S.-C., and Gleason, J. F. (2010). Recent large reduction in sulfur dioxide emissions from chinese power plants observed by the ozone monitoring instrument. *Geophysical Research Letters*, 37(8).

Liu, F., Page, A., Strode, S. A., Yoshida, Y., Choi, S., Zheng, B., Lamsal, L. N., Li, C., Krotkov, N. A., Eskes, H., et al. (2020). Abrupt decline in tropospheric nitrogen dioxide over china after the outbreak of covid-19. *Science Advances*, page eabc2992.

Liu, Y., Hu, C., Zhan, W., Sun, C., Murch, B., and Ma, L. (2018). Identifying industrial heat sources using time-series of the viirs nightfire product with an object-oriented approach. *Remote Sensing of Environment*, 204:347–365.

Lorente, A., Boersma, K., Eskes, H., Veefkind, J., Van Geffen, J., De Zeeuw, M., van der Gon, H. D., Beirle, S., and Krol, M. (2019). Quantification of nitrogen oxides emissions from build-up of pollution over paris with tropomi. *Scientific reports*, 9(1):1–10.

Ma, C., Yang, J., Chen, F., Ma, Y., Liu, J., Li, X., Duan, J., and Guo, R. (2018). Assessing heavy industrial heat source distribution in china using real-time viirs active fire/hotspot data. *Sustainability*, 10(12):4419.

Mallik, C. and Lal, S. (2014). Seasonal characteristics of so 2, no 2, and co emissions in and around the indo-gangetic plain. *Environmental monitoring and assessment*, 186(2):1295–1310.

Matthias, V., Arndt, J. A., Aulinger, A., Bieser, J., Denier van der Gon, H., Kranenburg, R., Kuenen, J., Neumann, D., Pouliot, G., and Quante, M. (2018). Modeling emissions for three-dimensional atmospheric chemistry transport models. *Journal of the Air & Waste Management Association*, 68(8):763–800.

Mennen, M. G., Mooij, M., and van Dijk, J. (2008). Inventarisatie co-emissies uit de industrie: emissiereductiedoelstelling loslaten? *RIVM rapport 680177001*.

Ministry of Steel (2019). Annual report 2018-2019. Accessed at 21-09-2020. Obtained from `https://steel.gov.in/sites/default/files/MoS$%$20AR$%$20Eng.pdf`.

Mortier, R. (2020). Personal Communication. Manager Environmental Department, ArcelorMittal Gent.

Nigam, S., Nigam, R., Kulshrestha, M., and Mittal, S. K. (2010). Carbon monoxide modeling studies: a review. *Environmental Reviews*, 18(NA):137–158.

Otsu, N. (1979). A threshold selection method from gray-level histograms. *IEEE transactions on systems, man, and cybernetics*, 9(1):62–66.

Pandey, S., Gautam, R., Houweling, S., Van Der Gon, H. D., Sadavarte, P., Borsdorff, T., Hasekamp, O., Landgraf, J., Tol, P., Van Kempen, T., et al. (2019). Satellite observations reveal extreme methane leakage from a natural gas well blowout. *Proceedings of the National Academy of Sciences*, 116(52):26376–26381.

Pregger, T. and Friedrich, R. (2009). Effective pollutant emission heights for atmospheric transport modelling based on real-world information. *Environmental Pollution*, 157(2):552–560.

Pulles, T. (2008). Quality of emission data: Community right to know and national reporting. *Environmental Sciences*, 5(3):151–160.

Raub, J. A., Mathieu-Nolf, M., Hampson, N. B., and Thom, S. (2000). Carbon monoxide poisoning—a public health perspective. *Toxicology*, 145(1):1–14.

Reuter, M., Buchwitz, M., Schneising, O., Krautwurst, S., O'Dell, C. W., Richter, A., Bovensmann, H., and Burrows, J. P. (2019). Towards monitoring localized co 2 emissions from space: co-located regional co 2 and no 2 enhancements observed by the oco-2 and s5p satellites. *Atmospheric Chemistry and Physics*, 19(14):9371–9383.

Saarinen, K. (2003). A method to improve the international comparability of emission data from industrial installations. *Environmental Science & Policy*, 6(4):355–366.

Saha, P. K., Borgefors, G., and di Baja, G. S. (2017). Skeletonization and its applications–a review. In *Skeletonization*. Elsevier.

SAIL (2020a). About bhilai steel plant. Accessed at 21-09-2020. Obtained from `https://sail.co.in/bhilai-steel-plant/about-bhilai-steel-plant`.

SAIL (2020b). About durgapur steel plant. Accessed at 21-09-2020. Obtained from `https://sail.co.in/durgapur-steel-plant/about-durgapur-steel-plant`.

Schneising, O., Buchwitz, M., Reuter, M., Bovensmann, H., Burrows, J., Borsdorff, T., Deutscher, N. M., Feist, D., Griffith, D. W., Hase, F., et al. (2019). A scientific algorithm to simultaneously retrieve carbon monoxide and methane from tropomi onboard sentinel-5 precursor.

Schroeder, W. and Giglio, L. (2018). Nasa viirs land science investigator processing system (sips) visible infrared imaging radiometer suite (viirs) 375 m & 750 m active fire products: product user?s guide version 1.4.

Seinfeld, J. H. and Pandis, S. N. (2016). *Atmospheric chemistry and physics: from air pollution to climate change*. John Wiley & Sons.

Severstal (2020). Cherepovets steel mill. Accessed at 21-09-2021. Obtained from `https://www.severstal.com/eng/about/businesses/chermk`.

Sharan, M., Yadav, A. K., Singh, M., Agarwal, P., and Nigam, S. (1996). A mathematical model for the dispersion of air pollutants in low wind conditions. *Atmospheric Environment*, 30(8):1209–1220.

Shatokha, V., Matukhno, E., Belokon, K., and Shmatkov, G. (2020). Potential means to reduce co 2 emissions of iron and steel industry in ukraine using best available technologies. *Journal of Sustainable Metallurgy*, pages 1–12.

Shindell, D., Faluvegi, G., Stevenson, D., Krol, M., Emmons, L., Lamarque, J.-F., Pétron, G., Dentener, F., Ellingsen, K., Schultz, M., et al. (2006). Multimodel simulations of carbon monoxide: Comparison with observations and projected near-future changes. *Journal of Geophysical Research: Atmospheres*, 111(D19).

Spichtinger, N., Damoah, R., Eckhardt, S., Forster, C., James, P., Beirle, S., Wagner, T., Novelli, P., and Stohl, A. (2004). Boreal forest fires in 1997 and 1998: a seasonal comparison using transport model simulations and measurement data. *Atmospheric Chemistry and Physics, European Geosciences Union*, pages 1857–1868.

Streets, D. G., Canty, T., Carmichael, G. R., de Foy, B., Dickerson, R. R., Duncan, B. N., Edwards, D. P., Haynes, J. A., Henze, D. K., Houyoux, M. R., et al. (2013). Emissions estimation from satellite retrievals: A review of current capability. *Atmospheric Environment*, 77:1011–1042.

Streets, D. G., Zhang, Q., Wang, L., He, K., Hao, J., Wu, Y., Tang, Y., and Carmichael, G. R. (2006). Revisiting china's co emissions after the transport and chemical evolution over the pacific (trace-p) mission: Synthesis of inventories, atmospheric modeling, and observations. *Journal of Geophysical Research: Atmospheres*, 111(D14).

Tang, M. and Mudd, G. M. (2014). Canadian power stations and the national pollutant release inventory (npri): a success story for pollution intensity? *Water, Air, & Soil Pollution*, 225(10):2129.

Thompson, D. R., Karpatne, A., Ebert-Uphoff, I., Frankenberg, C., Thorpe, A. K., Bue, B. D., and Green, R. O. (2017). Isgeo dataset jpl-ch4-detection-2017-v1. 0: A benchmark for methane source detection from imaging spectrometer data.

Trainer, M., Ridley, B., Buhr, M., Kok, G., Walega, J., Hübler, G., Parrish, D., and Fehsenfeld, F. (1995). Regional ozone and urban plumes in the southeastern united states: Birmingham, a case study. *Journal of Geophysical Research: Atmospheres*, 100(D9):18823–18834.

United Nations (2007). Guidance on implementation of the protocol on pollutant release and transfer registers. Technical report, United Nations Economic Commission for Europe.

van der Velde, I. R., van der Werf, G. R., Houweling, S., Eskes, H. J., Veefkind, J. P., Borsdorff, T., and Aben, I. (2020). Biomass burning combustion efficiency observed from space using measurements of co and no 2 by tropomi. *Atmospheric Chemistry and Physics Discussions*, pages 1–65.

Van Kempen, T. A., Van Hees, R. M., Tol, P. J., Aben, I., and Hoogeveen, R. W. (2019). In-flight calibration and monitoring of the tropospheric monitoring instrument (tropomi) short-wave infrared (swir) module. *Atmospheric Measurement Techniques*, 12(12):6827–6844.

Varon, D. J., Jacob, D. J., McKeever, J., Jervis, D., Durak, B. O., Xia, Y., and Huang, Y. (2018). Quantifying methane point sources from fine-scale satellite observations of atmospheric methane plumes. *Atmospheric Measurement Techniques*, 11(10).

Veefkind, J., Aben, I., McMullan, K., Förster, H., De Vries, J., Otter, G., Claas, J., Eskes, H., De Haan, J., Kleipool, Q., et al. (2012). Tropomi on the esa sentinel-5 precursor: A gmes mission for global observations of the atmospheric composition for climate, air quality and ozone layer applications. *Remote Sensing of Environment*, 120:70–83.

Vermeer, K. A., Vos, F. M., Lemij, H. G., and Vossepoel, A. M. (2004). A model based method for retinal blood vessel detection. *Computers in biology and medicine*.

Vidot, J., Landgraf, J., Hasekamp, O., Butz, A., Galli, A., Tol, P., and Aben, I. (2012). Carbon monoxide from shortwave infrared reflectance measurements: A new retrieval approach for clear sky and partially cloudy atmospheres. *Remote sensing of environment*, pages 255–266.

Wang, K., Tian, H., Hua, S., Zhu, C., Gao, J., Xue, Y., Hao, J., Wang, Y., and Zhou, J. (2016). A comprehensive emission inventory of multiple air pollutants from iron and steel industry in china: Temporal trends and spatial variation characteristics. *Science of the Total Environment*, 559:7–14.

White, W., Anderson, J., Blumenthal, D., Husar, R., Gillani, N., Husar, J., and Wilson, W. (1976). Formation and transport of secondary air pollutants: ozone and aerosols in the st. louis urban plume. *Science*, 194(4261):187–189.

Wofsy, S. C., McConnell, J. C., and McElroy, M. B. (1972). Atmospheric ch4, co, and co2. *Journal of Geophysical Research*, 77(24):4477–4493.

World Health Organization (2016). Ambient air pollution: A global assessment of exposure and burden of disease.

Yadav, I. C., Devi, N. L., Li, J., Syed, J. H., Zhang, G., and Watanabe, H. (2017). Biomass burning in indochina peninsula and its impacts on regional air quality and global climate change-a review. *Environmental Pollution*, 414–427.

Zhang, T. and Suen, C. Y. (1984). A fast parallel algorithm for thinning digital patterns. *Communications of the ACM*.

Zhou, Y., Zhao, F., Wang, S., Liu, W., and Wang, L. (2018). A method for monitoring iron and steel factory economic activity based on satellites. *Sustainability*, 10(6):1935.